Spectroscopic and Theoretical Study on Siloxy-Based Molybdenum and Tungsten Alkylidyne Catalysts for Alkyne Metathesis

Alexander Haack, Julius Hillenbrand, Maurice van Gastel, Alois Fürstner,* Frank Neese*

Max-Planck-Institut für Kohlenforschung, 45470 Mülheim/Ruhr, Germany

*Email: *neese@kofo.mpg.de*, *fuerstner@kofo.mpg.de*

Supporting Information

Contents

GENERAL

Unless stated otherwise, all reactions were carried out under Ar in flame-dried glassware. The solvents and commercially available compounds (Aldrich) used were purified by distillation over the drying agents indicated and were transferred under Ar: Et_2O (CaH_2), THF (Mg/anthracene), toluene ((Na/K), *n*-pentane (Na/K), $C_6D_5CD_3$ (3Å MS) and 3-hexyne (3Å MS). Compounds **S2**, **S4, S5** and **3-CAr** were prepared as described in the literature.[1, 2] The molecular sieves used in this investigation were dried for 24 h at 150 °C (sand bath) under vacuum prior to use and were stored and transferred under argon atmosphere.

IR: Spectrum One (Perkin-Elmer) spectrometer, wavenumbers ($\tilde{\nu}$) in cm^{-1}.
MS (EI): Finnigan MAT 8200 (70 eV), ESI-MS: ESQ3000 (Bruker), accurate mass determinations: Bruker APEX III FT-MS (7 T magnet) or Mat 95 (Finnigan). Elemental analysis: H. Kolbe, Mülheim/Ruhr.

NMR spectra were acquired on Bruker AvanceIII 300, 400, 500 MHz or an AvanceNeo 600 MHz NMR spectrometer in the solvents indicated; chemical shifts (δ) are given in ppm relative to TMS, coupling constants (*J*) in Hz. The solvent signals were used as references and the chemical shifts converted to the TMS scale ($CDCl_3$: $\delta_C \equiv 77.0$ ppm; residual $CHCl_3$ in $CDCl_3$: $\delta_H \equiv 7.26$ ppm; CD_2Cl_2: $\delta_C \equiv 53.8$ ppm; residual ^1H: $\delta_H \equiv 5.32$ ppm; $C_6D_5CD_3$: $\delta_C \equiv 20.7$ ppm; residual $D_5C_6CD_2H$: $\delta_H = 2.09$ ppm). Chemical shifts were referenced indirectly to the ^1H chemical shift of the solvent.[3]

EXPERIMENTAL DATA

Complex S1

A 100 mL Schlenk flask was equipped with a magnetic stir bar and was flame dried under vacuum. The

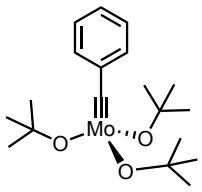

flask was filled with argon and Mo(≡CPh)Br_3(dme) (**S2**) (1.20 g, 2.20 mmol) was dissolved in THF (25 mL). Then a solution of NaO*t*Bu (633 mg, 6.59 mmol) in THF (10 mL) was added dropwise at 25°C to the stirred solution. Stirring was continued for 14 h at ambient temperature before the solvent was removed *in vacuo* to obtain a dark brown solid. A second, flame dried 50 mL Schlenk flask was equipped with a magnetic stir bar and a Celite® (2 cm) packed argon frit. The dark brown solid was suspended in *n*-pentane (4 x 5 mL) and was filtered through the Celite® pad. The resulting filtrate was concentrated and the residue dried under vacuum (10^{-3} mbar) to give complex **S1** as a brown solid (717 mg, 80%) free of any residual THF. ^1H NMR (400 MHz, C_6D_6): δ = 7.52 – 7.49 (m, 2H), 7.13 – 7.07 (m, 2H), 6.88 (tt, *J* = 7.2, 1.3 Hz, 1H), 1.49 (s, 27H). ^{13}C NMR (101 MHz, C_6D_6): δ = 276.6, 146.7, 129.7, 128.4, 127.0, 80.3, 32.8. ^{95}Mo NMR (26

MHz, 60°C, $C_6D_5CD_3$): δ = 62.0. The analytical and spectroscopic data are in agreement with those reported in the literature.[4]

Complex S3

A 250 mL Schlenk flask was equipped with a magnetic stir bar and flame dried under vacuum. The flask

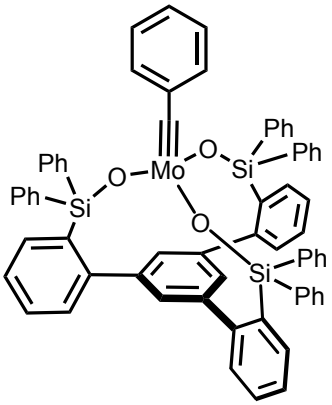

was filled with argon and charged with ligand **S4** (964 mg, 1.07 mmol), which was azeotropically dried with benzene (3 x 5 mL) to remove residual water. Toluene (81 mL) was added and the mixture vigorously stirred for 10 min to obtain a clear solution. Then a solution of complex **S1** (454 mg, 1.12 mmol) in toluene (16 mL) was added dropwise and stirring was continued for 3 h at ambient temperature. The solvent was removed *in vacuo* and the yellow/orange solid was washed with *n*-pentane (3 x 5 mL) and Et_2O (3 x 5 mL) to give a yellow/orange powder containing crude mixture of **S3**/[**S3**]$_2$ (1.14 g, 98%). A 10 mL Schlenk flask was equipped with a magnetic stir bar and flame dried under vacuum. The flask was filled with argon and charged with the crude mixture of **S3**/[**S3**]$_2$ (70.0 mg, 64.6 µmol) and $C_6D_5CD_3$ (1 mL) to give a yellow suspension. The mixture was vigorously stirred at 60°C for 1 h to give an orange solution containing only monomeric complex **S3**. ^{1}H NMR (600 MHz, $C_6D_5CD_3$): δ = 7.81 – 7.77 (m, 12H), 7.75 – 7.73 (m, 3H), 7.25 (s, 3H), 7.12 – 7.06 (m, 12H), 7.06 – 7.01 (m, 12H), 6.89 – 6.85 (m, 3H), 6.58 (t, *J* = 7.7 Hz, 2H), 6.49 (tt, *J* = 6.9, 1.1 Hz, 1H), 6.24 – 6.19 (m, 2H). ^{13}C NMR (151 MHz, $C_6D_5CD_3$): δ = 310.7, 149.5, 146.3, 144.1, 138.0, 137.4, 135.3, 135.0, 130.5, 130.1, 129.8, 129.3, 128.6, 128.2, 127.3, 127.2, 126.2, 20.4. ^{29}Si NMR (79 MHz, $C_6D_5CD_3$): δ = −9.6. ^{95}Mo NMR (26 MHz, 60°C, $C_6D_5CD_3$): δ = 377.2. IR (film): $\tilde{\nu}$ 3045, 1583, 1484, 1427, 1409, 1261, 1112, 1063, 1029, 1001, 871, 830, 759, 738, 696, 622, 566, 548, 528, 506, 464 cm^{-1}. HRMS-ESI (m/z): calculated for $C_{67}H_{50}MoO_3Si_3^+$ $[M]^+$, 1084.21163; found, 1084.212010. Elemental analysis (%) calculated for $C_{67}H_{50}MoO_3Si_3$: C 74.28, H 4.65, Mo 8.86, Si 7.78; found: C 74.31, H 4.67, Mo 8.80, Si 7.71.

Complex 2-MTd

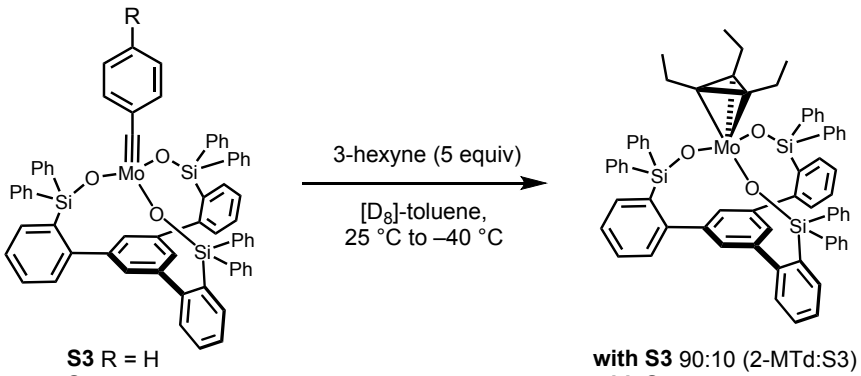

S3 R = H
S5 R = OMe

with S3 90:10 (2-MTd:S3)
with S5 93:7 (2-MTd:S5)

A 10 mL Schlenk flask was equipped with a magnetic stir bar and was flame dried under vacuum. The flask was filled with argon, charged with [**S5**]$_2$ (13.5 mg, 0.012 mmol) and suspended in $C_6D_5CD_3$ (0.6 mL) to give a yellow suspension. A flame dried *J. Young* NMR tube was filled with argon, charged with this suspension and heated to 60°C until full conversion to monomeric complex **108** was observed. After cooling to 25°C, 3-hexyne (6.9 µL, 61 µmol) was added to the yellow solution and an instant color change to black was observed. The full characterization of **147** was conducted by NMR spectroscopy at 25°C. ^{1}H NMR (600 MHz, $C_6D_5CD_3$): δ = 7.81 – 7.76 (m, 12H), 7.68 – 7.64 (m, 3H), 7.27 (s, 3H), 7.18 – 7.13 (m, 6H), 7.10 – 7.06 (m, 12H), 6.93 – 6.89 (m, 3H), 7.13 – 6.98 (m, 6H), 1.75 (m, 6H), 0.48 (t, *J* = 7.4 Hz, 9H). ^{13}C NMR (151 MHz, $C_6D_5CD_3$): δ = 150.3, 144.0, 139.1, 137.2, 136.7, 135.2, 129.6, 129.3, 129.2, 128.3, 127.4, 125.2, 83.9, 18.5, 15.4. ^{29}Si NMR (119 MHz, $C_6D_5CD_3$): δ = -8.48. The spectroscopic data are in agreement with those reported in the literature.[2, 5]

A 10 mL Schlenk flask was equipped with a magnetic stir bar and was flame dried under vacuum. The flask was filled with argon, charged with [**S3**]$_2$ (11.3 mg, 0.010 mmol) and suspended in $C_6D_5CD_3$ (0.5 mL) to give a yellow suspension. A flame dried *J. Young* NMR tube was filled with argon, charged with this suspension and heated to 60°C until full conversion to monomeric complex **S3** was observed. After cooling to 25°C, 3-hexyne (5.9 µL, 52 µmol) was added to the yellow solution and an instant color change to black was observed. A variable-temperature NMR study was conducted from 25°C to -70°C (***Figure S1***).

A)

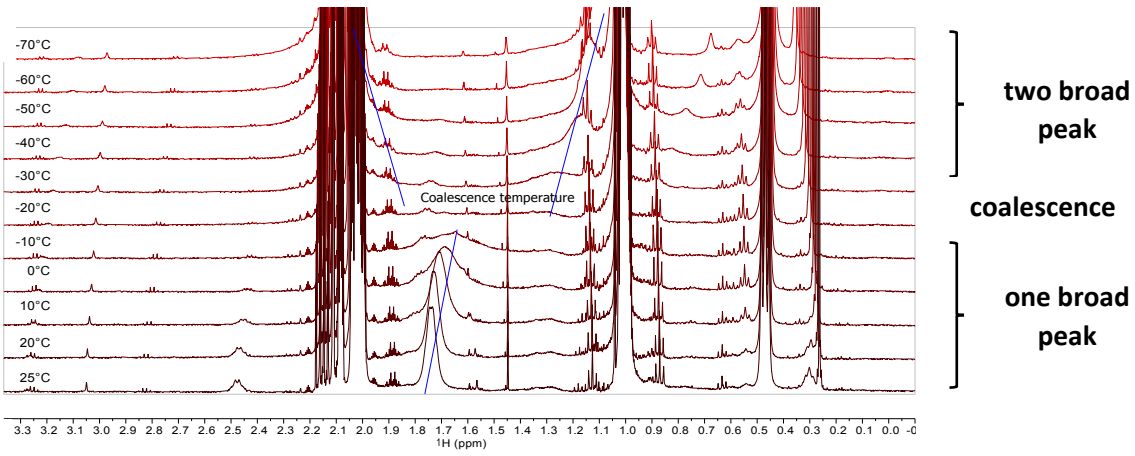

B)

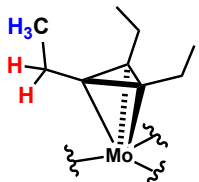

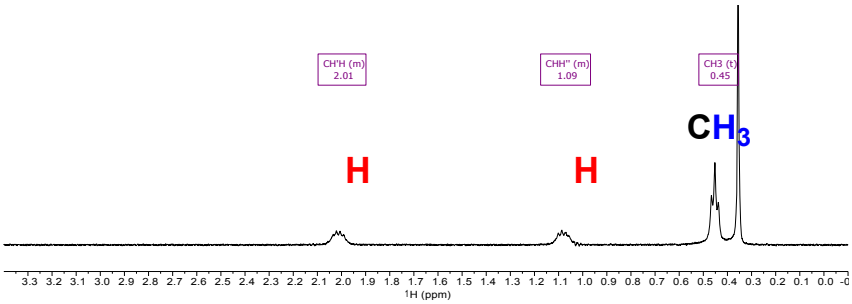

Figure S1. A.) Low-temperature ^{1}H NMR study of **2-MTd** from 25 °C to −70 °C in [D_8]-toluene; B.) 1D selective NOESY NMR of **2-MTd** obtained upon excitation of the CH_3 group at -70 °C; methylene protons in red; methyl group in blue.

NMR Investigation of Reaction of Catalysts 3-CAr with 3-Hexyne

A 10 mL Schlenk flask was equipped with a magnetic stir bar and was flame dried under vacuum. The flask was filled with argon, charged with **3-CAr** (11.6 mg, 0.016 mmol) and dissolved in $C_6D_5CD_3$ (0.5 mL) to give an orange solution. A flame dried *J. Young* NMR tube was filled with argon and the solution was transferred to the NMR tube. A ^{1}H NMR spectrum of this solution was acquired (***Figure S2*** A) and then 3-hexyne (8.9 µL, 79 µmol) was added to it. The ^{1}H NMR spectrum at 25 °C revealed that the major species is dissociated complex **3-CAr** and small quantities of a new, dynamic species were detected (***Figure S2*** **B** and insert).

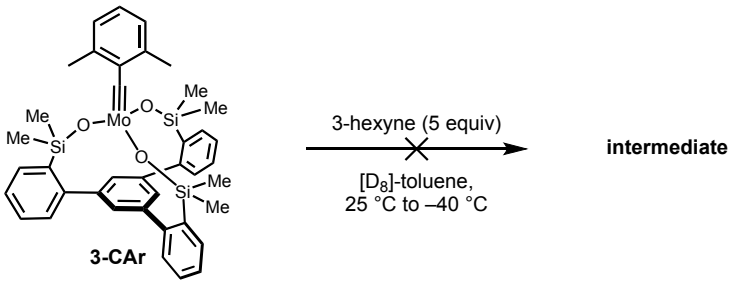

Although cooling to −40 °C improved the quality of the broad signals (3.0 – 3.7 ppm) in the ^{1}H NMR spectrum, we were not able to detect any ^{1}H, ^{13}C HMBC NMR signals to determine the composition of the dynamic species (***Figure S2*** **C** and insert).

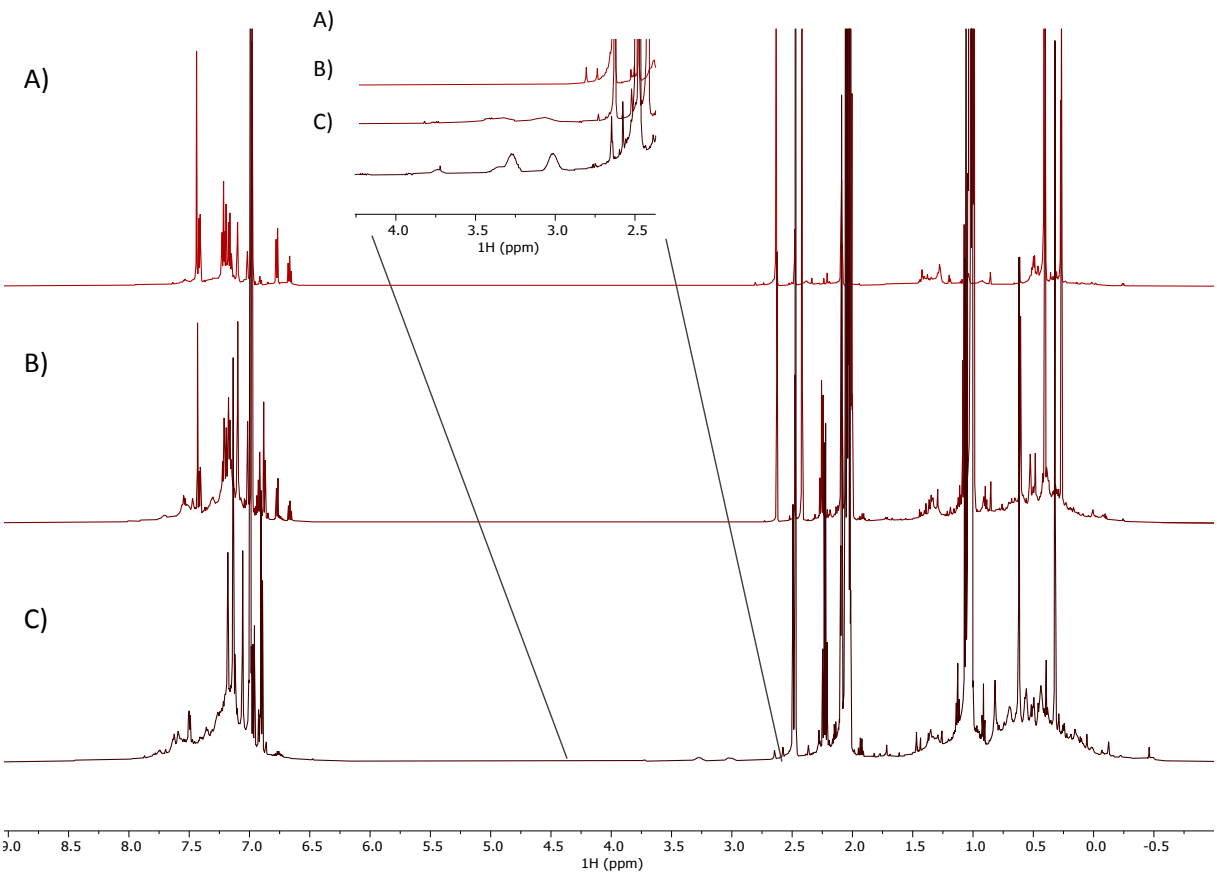

Figure S2. A) ^{1}H NMR of complex **3-CAr** in $C_6D_5CD_3$ at 25 °C. B) ^{1}H NMR of complex **3-CAr** with 5 equiv of 3-hexyne in $C_6D_5CD_3$ at 25 °C. C) ^{1}H NMR of complex **3-CAr** with 5 equiv of 3-hexyne in $C_6D_5CD_3$ at −40 °C, insert shows small quantities of a dynamic species.

Geometry of Complexes

Comparison between XRay and DFT results

Table S1: Geometry Comparison between X-ray [LEKFOY] *and DFT optimized structure of* ***1-CAr***

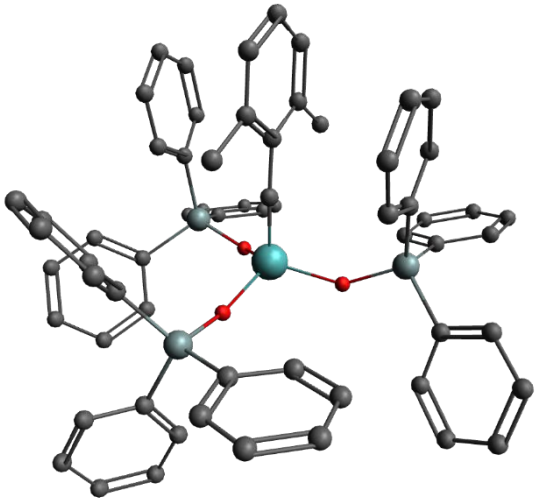

	X-ray	DFT
B(Mo≡C)	1.748(2)	1.753
A(Mo-C-C)	171.4(1)	172.8
B(Mo-O)	1.885(1)	1.892
D(O-Mo-O-O)	132.40(6)	127.4
A(C-Mo-O)	103.3(1), 103.4(1), 108.5(1)	105
A(Mo-O-Si)	146.4(1), 154.1(1), 169.4(1)	138, 140, 160
B(O-Si)	1.65(1), 1.65(1), 1.63(1)	1.67, 1.67, 1.65
D(C-Mo-O-Si)	1.2(1), 4.4(2), 98.3(4)	48, 6, 14

Table S2: Geometry Comparison between X-ray [PUVZUE] *and DFT optimized structure of* ***2-CAr***

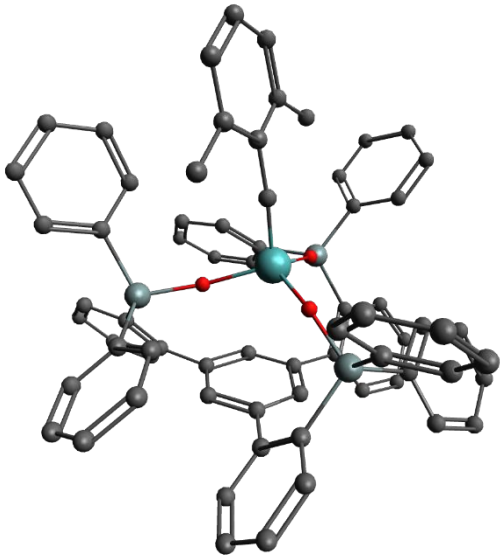

	X-ray	DFT
B(Mo≡C)	1.742(2)	1.753
A(Mo-C-C)	177.1(1)	174.5
B(Mo-O)	1.8811(13), 1.8797(13), 1.8984(14)	1.89, 1.87, 1.89
D(O-Mo-O-O)	137.20(9)	133.5
A(C-Mo-O)	103.42(8), 103.23(8), 102(61(8)	104
A(Mo-O-Si)	170.55(9), 164.40(8), 156.20(9)	154, 163, 156
B(O-Si)	1.6320(14), 1.6338(15), 1.6351(15)	1.648
D(C-Mo-O-Si)	105.0(6), 124.0(4), 147.2(3)	160, 49, 109

Table S3: Geometry Comparison between X-ray [IPUXAV] *and DFT optimized structure of* ***1-MCBD****. C_α refers to the carbons directly bonded to the molybdenum, the subscripts ax and eq on the oxygen atoms refer to the trigonal-bipyramidal ligand coordination.*

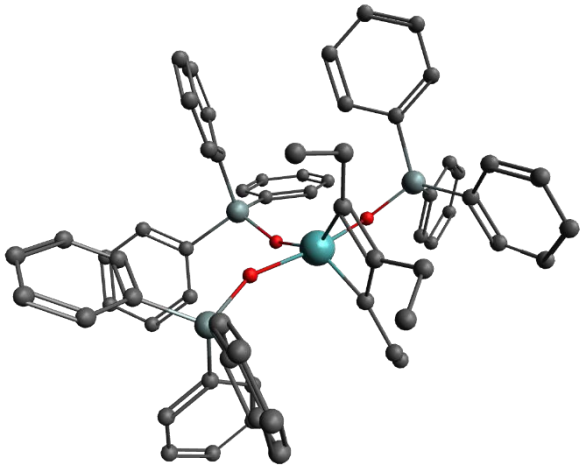

	X-ray	DFT
B(Mo-C_α)	1.882(2), 1.896(2)	1.90
B(Mo-C_β)	2.117(2)	2.133
A(C_α-Mo-C_α)	83.95(10)	83.3
A(C_α-C_β-C_α)	120.73(19)	121.0
A(O_{eq}-Mo-C_α)	143.38(8), 132.65(8)	141.3, 135.3
A(O_{eq}-Mo-C_β)	175.30(8)	176.5
B(Mo-O)	ax: 2.0043(13), 2.0000(13) eq: 1.9030(15)	ax: 2.00, eq: 1.919
A(O_{ax}-Mo-O_{eq})	84.58(6), 82.46(6)	84.2, 82.5
D(O_{ax}-Mo-O_{eq}-O_{ax})	173.21(6)	177.3
A(Mo-O-Si)	ax: 145.14(9), 147.86(9), eq: 142.61(9)	ax: 145, 154, eq: 145
B(O-Si)	ax: 1.6051(14), 1.6070(14), eq: 1.6268(15)	ax: 1.630, eq: 1.654

Table S4: Geometry Comparison between X-ray [QOSTIE] *and DFT optimized structure of* ***2-MTd***

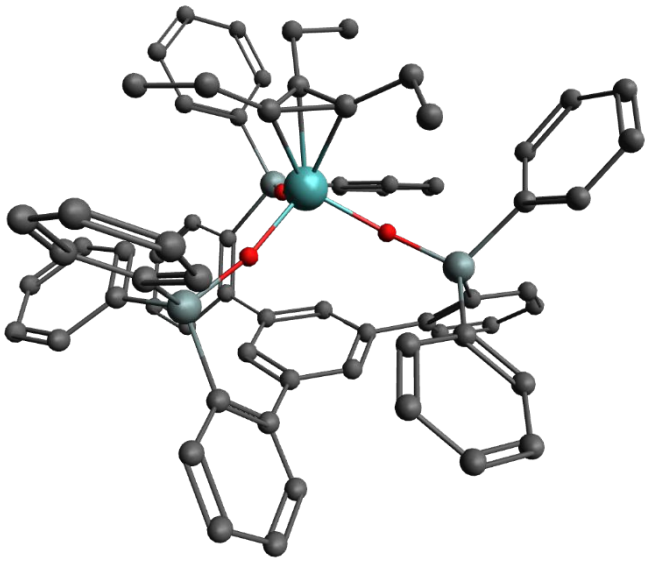

	X-ray	DFT
B(Mo-C)	2.058(5), 2.0645(5), 2.065(5)	2.066
D(C-Mo-C-C)	64.8(3)	64.7
B(Mo-O)	1.891(3), 1.897(3), 1.907(3)	1.912
A(C-Mo-O)	92.42(15), 92.92(17), 93.52(16)	93.0
A(O-Mo-O)	100.73(12), 100.95(13), 101.90(13)	101.1
D(O-Mo-O-O)	103.8(1)	104.0
A(Mo-O-Si)	169.21(19), 170.20(18), 170.38(18)	168.6
B(O-Si)	1.619(3), 1.620(3), 1.629(3)	1.636
D(C-Mo-O-Si)	11(1), 15(1), 22(1)	40.9

Table S5: Geometry Comparison between X-ray [CAFDIA] *and DFT optimized structure of* ***4-MCBD'****. C_α refers to the carbons directly bonded to the molybdenum, the subscripts ax and eq on the oxygen atoms refer to the trigonal-bipyramidal ligand coordination (although the geometry is rather a square monopyramidal one).*

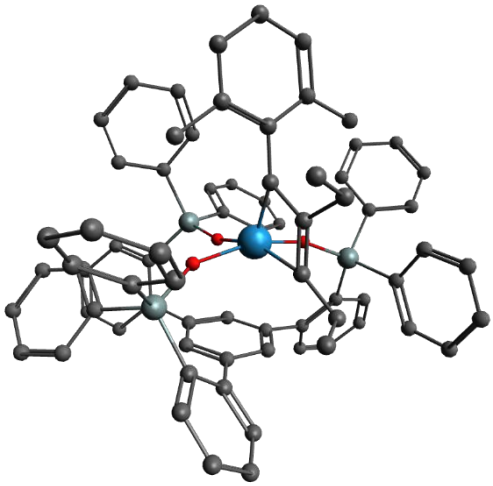

	X-ray	DFT
B(W-C_α)	α: 1.8730(17), α': 1.9648(15)	α: 1.894, α': 1.990
B(W-C_β)	2.1517(17)	2.172
A(C_α-W-C_α)	82.97(17)	82.2
A(C_α-C_β-$C_{\alpha'}$)	121.5(1)	122.0
A(O_{eq}-W-C_α)	α: 123.68(6), α': 153.20(6)	α: 120.9, α': 156.7
A(O_{eq}-W-C_β)	166.23(6)	163.2
A(W-O)	ax: 1.9516(12), 1.9883(12), eq: 1.9025(11)	ax: 1.98, eq: 1.935
A(O_{ax}-W-O_{eq})	85.08(5), 82.08(5)	84.8, 82.4
D(O_{ax}-W-O_{eq}-O_{ax})	166.44(5)	162.4
A(W-O-Si)	ax: 149.75(8), 153.86(8), eq: 155.25(8)	ax: 154, eq: 162.4
B(O-Si)	ax: 1.6066(13), eq: 1.6191(12), 1.6270(12)	ax: 1.63, eq: 1.648

Distortion PESs

To study the sterical stress imposed on the alkylidyne complexes by the different silanolate geometries, we turned to a small model system, i.e., $Mo(OSiH_3)_3(CMe)$. Varying the Mo-O-C angle/C-Mo-O-Si dihedral of all three groups simultaneously and recording the value of the respective other angle after reoptimization yields a potential energy surface (PES) showing two valleys (Figure S3). They correspond to the optimal combination of these two parameters. With the global minimum being at a Mo-O-Si angle of about 133° and a zero dihedral (concave geometry), **1-CEt** (blue data) lies close to the optimum. The basal arene forces the tripodal ligands to occupy large Mo-O-Si angles and consequently, they follow one of the valleys away from the global minimum. Interestingly, **2-CEt** (orange data) shows a larger variance of the three groups, while **3-CEt** (green data) is more homogeneous. The former mentioned "flat" ligand environment can thus be understood as being the optimal dihedrals for the given Mo-O-Si angle, enforced by the basal arene. The convex environment of **2-CEt** is probably due to the sterically more demanding phenyl-groups. However, the calculated electronic energies show the sterical stress is very similar for both tripodal systems and the more heterogeneous angles and dihedrals in **2-CEt** are not adding too much energy. This is probably because the dihedral is not well defined for such large angles.

We again used a model system, $Mo(OSiH_3)_3(C_3H_3)$, to study the sterical stress in the metallatetrahedrane configurations. Again, we recorded the PES of simultaneously changing all three Mo-O-Si angles or C-Mo-O-Si dihedrals (see Figure S4). The global minimum is, again, at a small angle (143°) and zero dihedral. While **1-MTd** and **3-MTd** occupy geometries close to the valley of larger dihedrals, **2-MTd** lies in the other valley, keeping the small dihedral and linearizing the angle. Despite these differences, the sterical stress is rather similar between all three complexes.

Interestingly, while the sterical stress decreases for the two tripodal complexes (approximately by the same amount), it increases for the monodentate system (compare Figure S3 and Figure S4Figure S3).

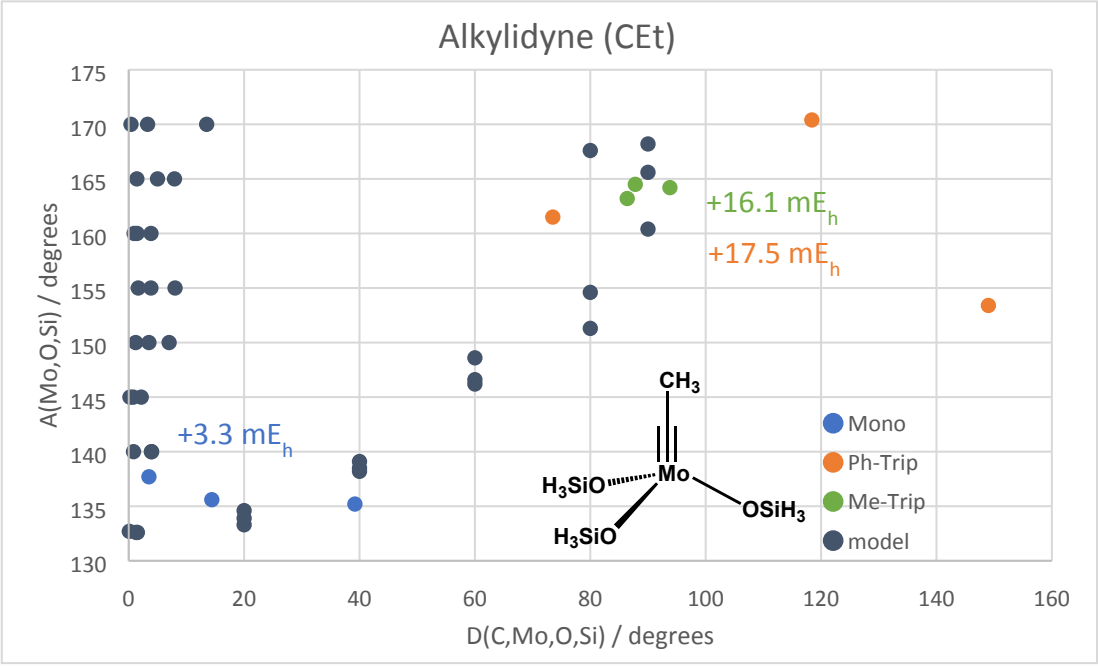

Figure S3: Alkylidyne model PES. The values for the three ligand bonds of each system are depicted as well. The electronic energies for the three systems are calculated by enforcing the model alkylidyne to occupy the same angle/dihedral values as in the actual complexes.

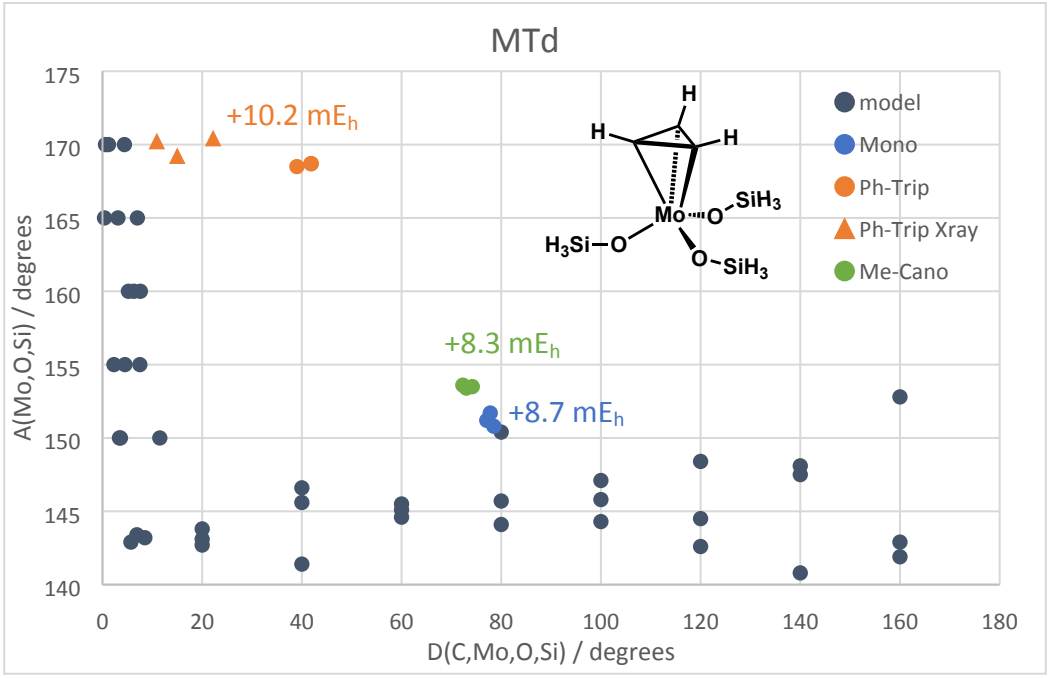

Figure S4: Metallatetrahedran model PES. The values for the three ligand bonds of each system are depicted as well. The electronic energies for the three systems are calculated by enforcing the model MTd to occupy the same angle/dihedral values as in the actual complexes.

preAdd complexes

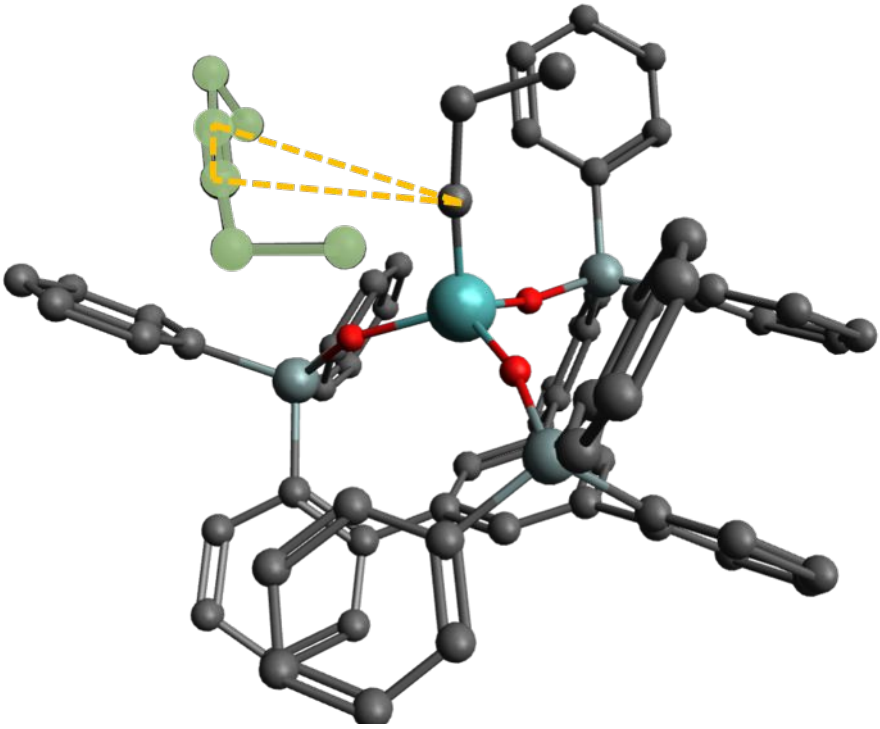

*Figure S5: preAdd complex of the **2-CEt** + 3-hexyne reaction system. The alkyne is only loosely bound and the alkylidyne complex is only marginally distorted.*

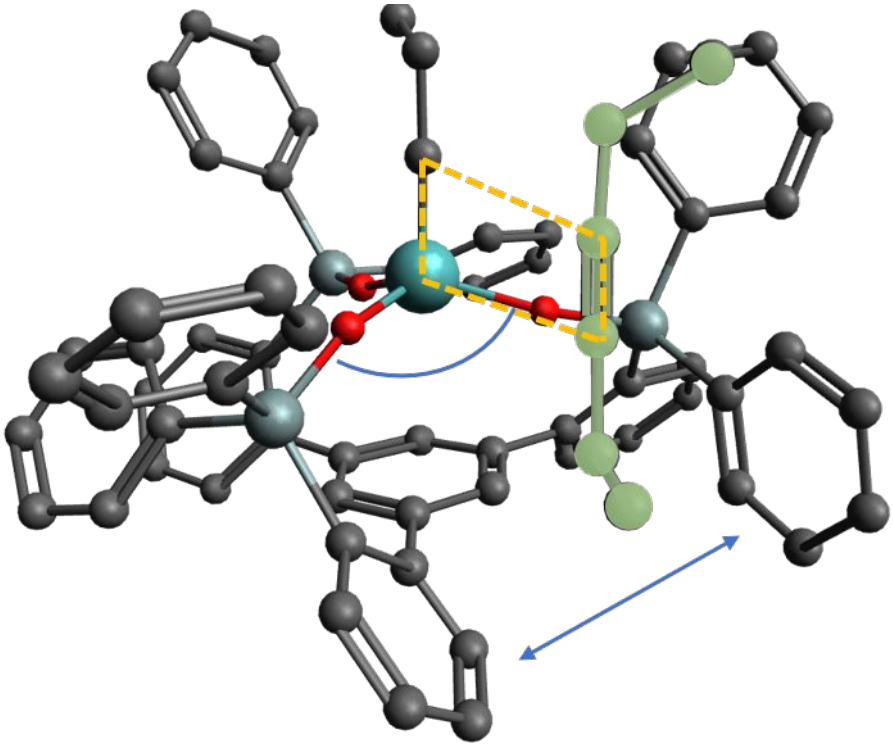

*Figure S6: preAdd2 complex of the **2-CEt** + 3-hexyne reaction system. The alkyne is placed between two silanolate phenyl groups, which's dispersion interaction had to be cleaved. The alignment of the alkyne and alkylidyne triple bond is close to parallel.*

Electronic Structure

Canonical MOs

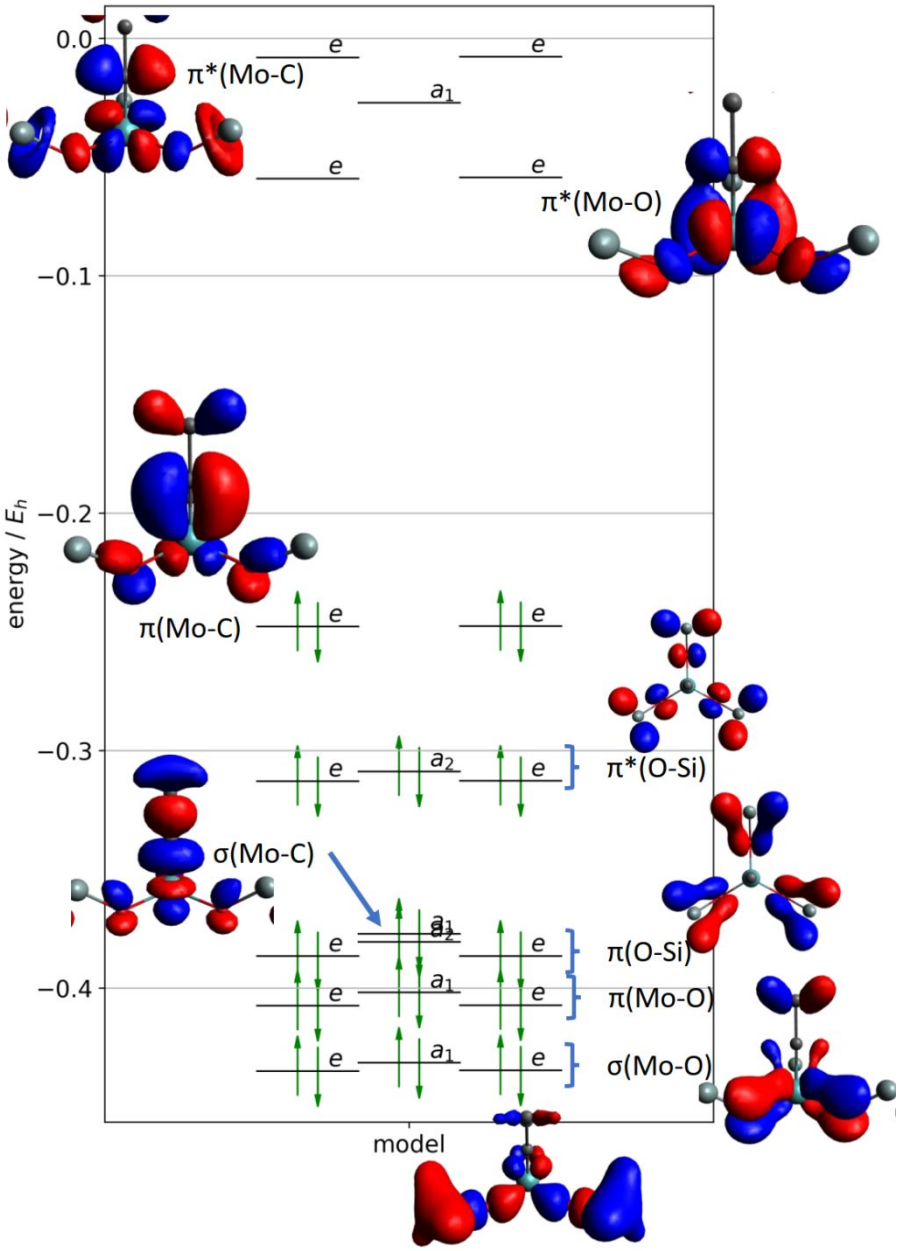

Figure S7: canonical MO diagram of the model alkylidyne complex $Mo(OSiH_3)_3(CMe)$ (C_{3v} symmetry).

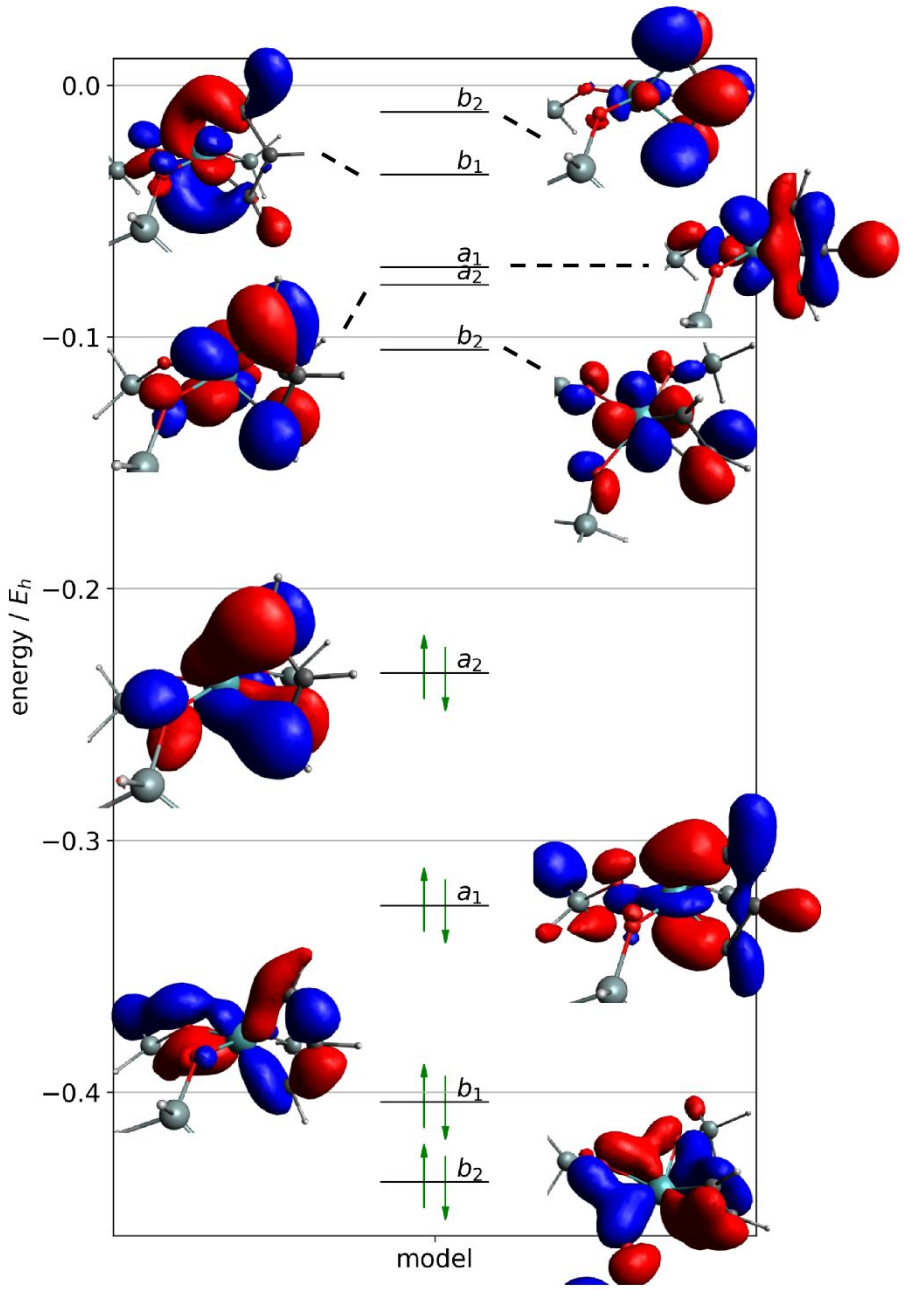

Figure S8: Canonical MO diagram of the model metallacyclobutadiene, $Mo(OSiH_3)_3(C_3H_3)$ (C_{2v} symmetry).

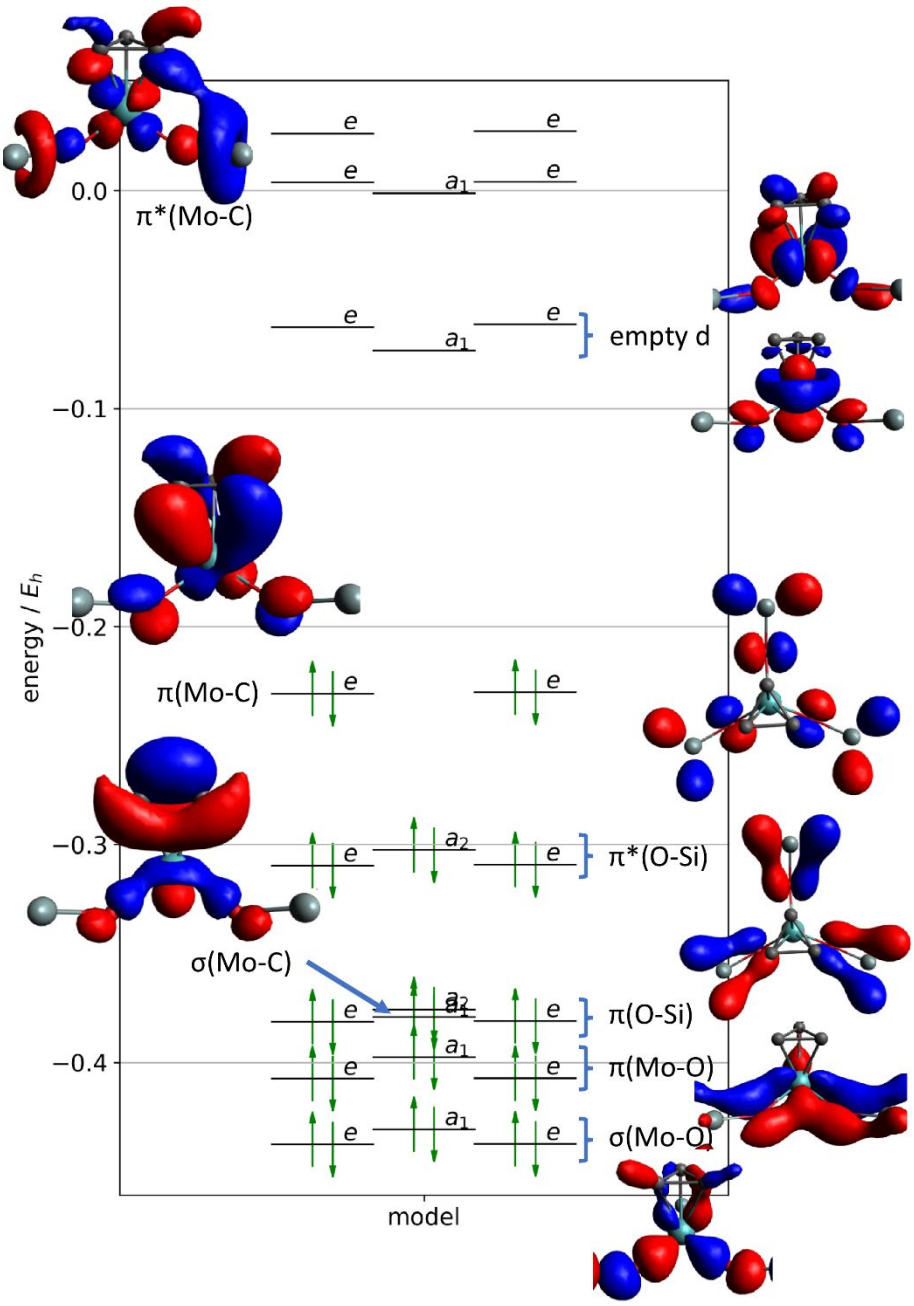

Figure S9: Canonical MO diagram of the metallatetrahedrane structure for the model complex $Mo(OSiH_3)_3(C_3H_3)$ (C_{3v} symmetry).

Localized MOs

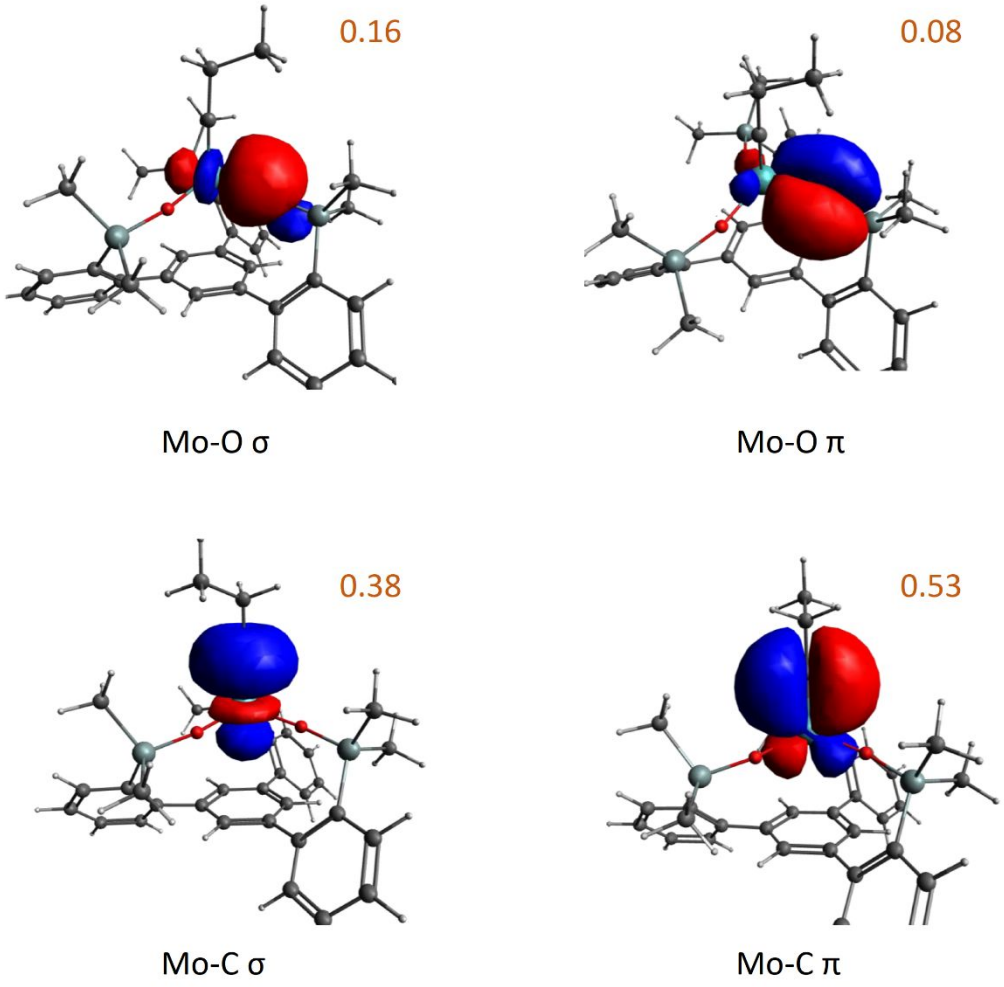

*Figure S10: Localized Molecular Orbitals (Pipek-Mezey algorithm) of the **3-CEt** complex, acting as example. The Mulliken Population at the molybdenum of the individual LMOs is also depicted. This is a measure of the amount of electron donation due to the respective orbital (0.5 corresponds to an equal share of the electrons, hence a non-polar covalent bond).*

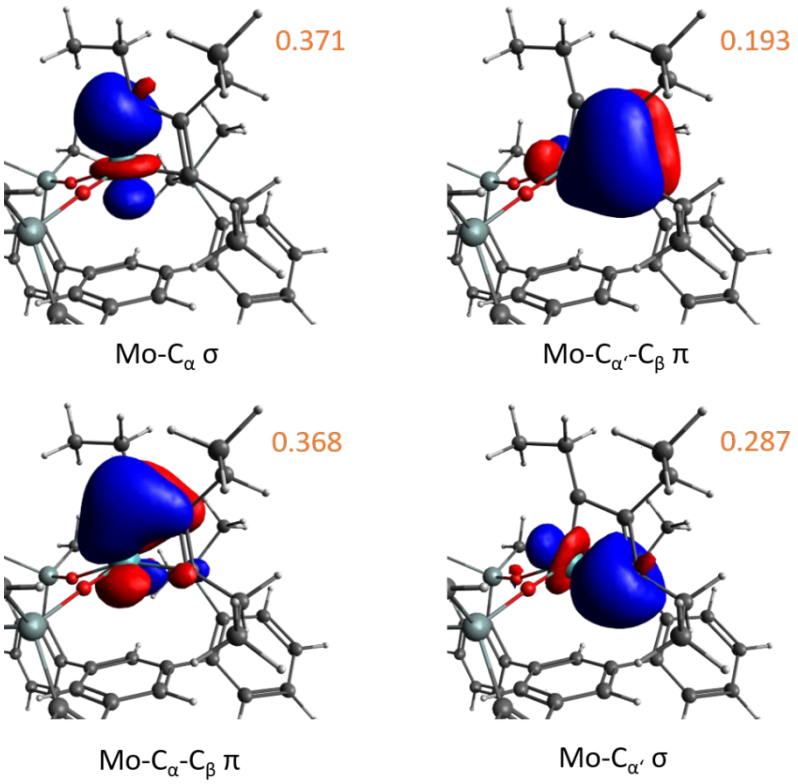

*Figure S11: Localized Molecular Orbitals (Pipek-Mezey algorithm) of the **3-MCBD** complex, acting as example. The Mulliken Population at the molybdenum of the individual LMOs is also depicted. This is a measure of the amount of electron donation due to the respective orbital (0.5 corresponds to an equal share of the electrons, hence a non-polar covalent bond).*

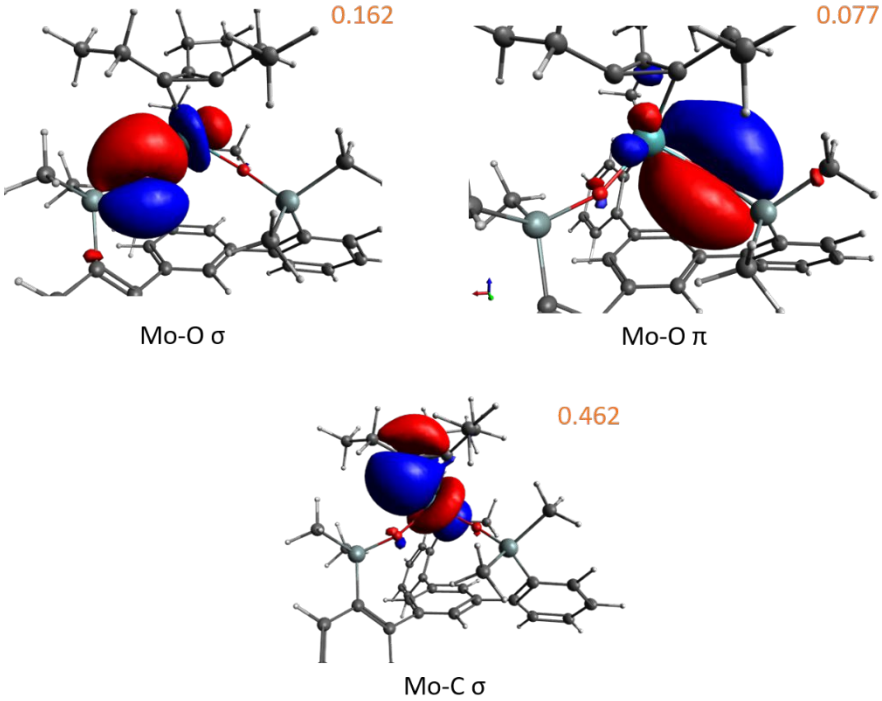

*Figure S12: Localized Molecular Orbitals (Pipek-Mezey algorithm) of the **3-MTd** complex, acting as example. The Mulliken Population at the molybdenum of the individual LMOs is also depicted. This is a measure of the amount of electron donation due to the respective orbital (0.5 corresponds to an equal share of the electrons, hence a non-polar covalent bond).*

Mayer Bond Orders

Table S6: Averaged Mayer bond orders and Loewdin partial charges for different propylidyne complexes.

	1-CEt	2-CEt	3-CEt	4-CEt
BO(M-C)	2.531	2.589	2.565	2.764
BO(M-O)	0.957	0.838	0.892	0.949
BO(O-Si)	0.945	0.952	1.018	0.984
q(M)	0.6751	0.6882	0.7334	0.7929

Table S7: Mayer Bond orders and Loewdin partial charges for different metallacyclobutadiene complexes.

	1-MCBD	2-MCBD	3-MCBD	4-MCBD
BO(M-C_α)	1.3198, 1.4490	1.1220, 1.4976	1.1128, 1.5434	1.2272, 1.5693
BO(C_α-C_β)	1.1981, 1.1635	1.1890, 1.0663	1.3319, 1.0367	1.2293, 0.9418
BO(M-C_β)	0.2467	0.3024	0.2841	0.6944
BO(M-O_a)	0.8454, 0.8297	0.7613, 0.7771	0.8317, 0.8440	0.7005, 0.7477
BO(M-O_t)	0.7452	0.7053	0.7856	0.8147
q(M)	0.734203	0.752787	0.778664	0.887939

Table S8: Averaged Mayer bond orders and Loewdin partial charges for different metallatetrahedran complexes

	1-MTd	2-MTd	3-MTd	4-MTd
BO(M-C)	0.828	0.844	0.857	0.955
BO(M-O)	0.802	0.733	0.820	0.882
BO(C-C)	0.756	0.734	0.750	0.770
BO(O-Si)	0.998	0.912	1.012	0.932
q(M)	0.744	0.748	0.781	0.926

NOCV/ETS results

Table S9: Contributions to E_{orb} from each NOCV pair. Values in kcal/mol. Only contribution larger than 2 kcal/mol are listed.

	MCBD		MTd	
NOCV pairs	Mo	W	Mo	W
1	-219.245	-290.983	-549.793	-639.048
2	-56.235	-46.167	-164.877	-173.109
3	-102.741	-145.373	-110.362	-151.145
4	-33.133	-31.603	-22.082	-44.893
5	-26.277	-41.632	-24.005	-32.572
6	-6.300	-6.743	-7.576	-14.569
7	-4.038	-4.495	-3.975	-4.827
8	-2.199	-2.823		

As seen in Table S9, some NOCV pairs are much more stabilizing in case of tungsten. For the more interesting case of the tungstenacyclobutadiene (**4-MCBD**), NOCV pairs 1, 3 and 5 are shown here, they all correspond to M-C σ-bonds. M-C π-bonds are more similar between the two metals.

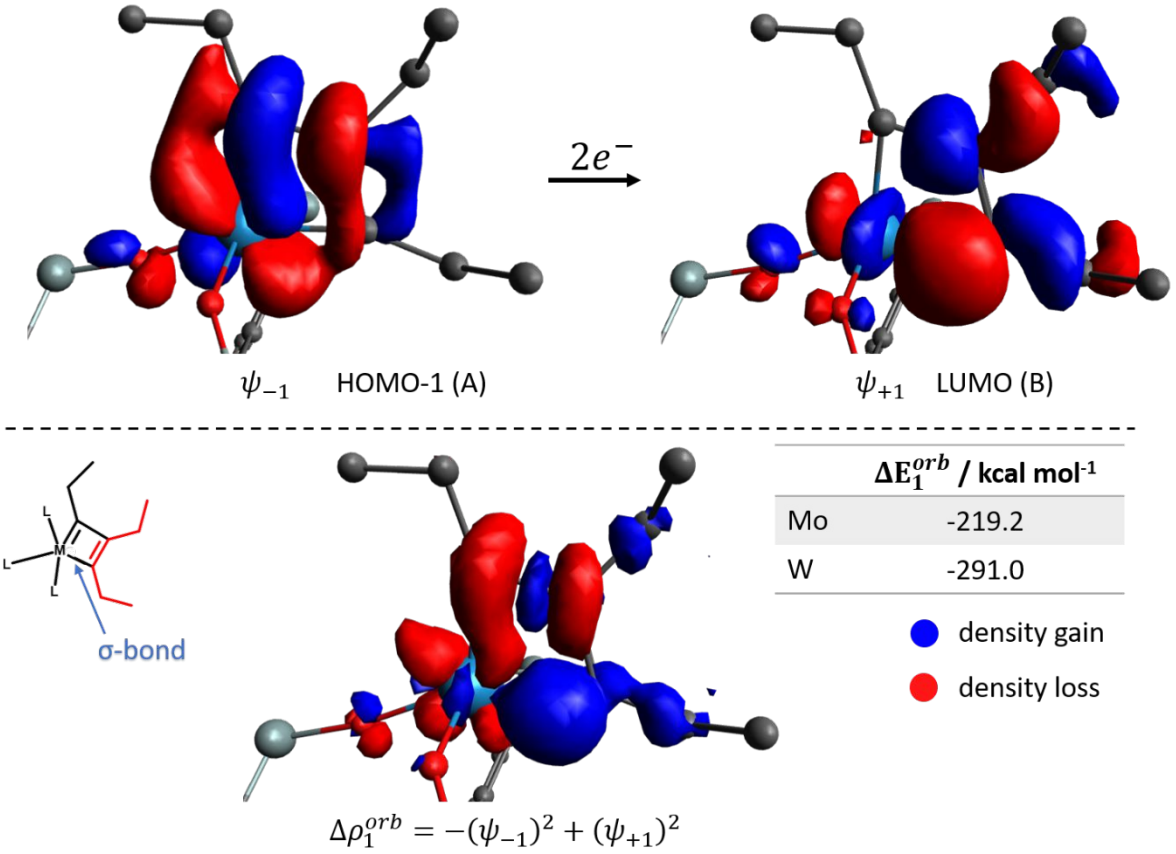

Figure S13: NOCV pair $\psi_{\pm 1}$ and the resulting difference density $\Delta\rho_1^{orb}$ for the metallacyclobutadienes. Fragment A = Alkylidyne, Framgent B = Alkyne.

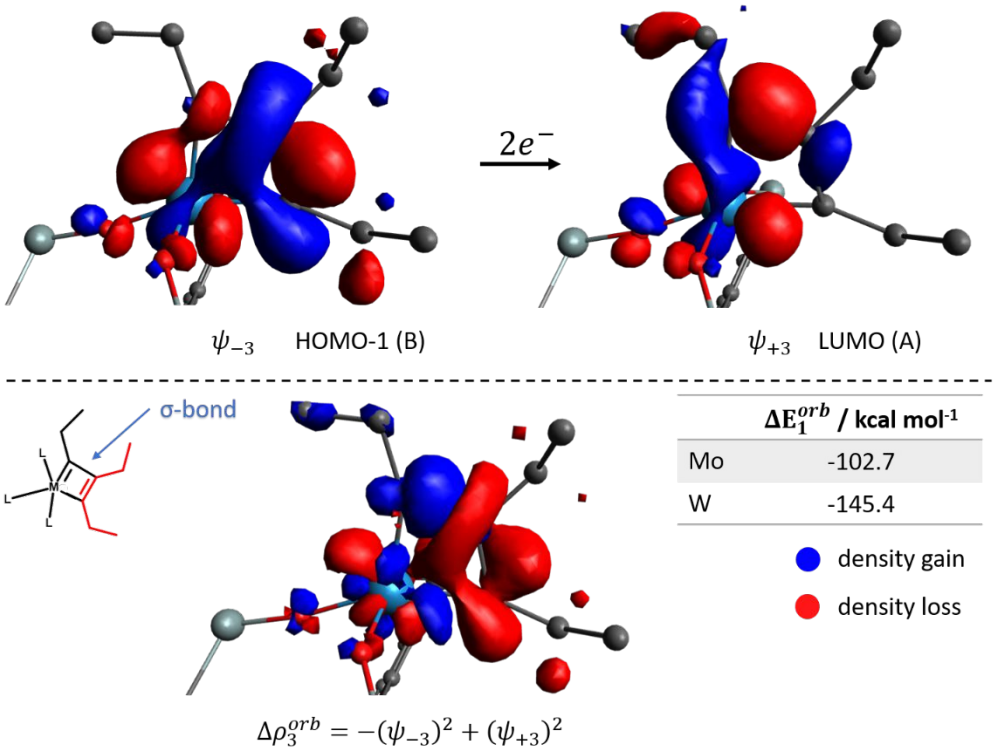

Figure S14: NOCV pair $\psi_{\pm 3}$ and the resulting difference density $\Delta\rho_3^{orb}$ for the metallacyclobutadienes. Fragment A = Alkylidyne, Framgent B = Alkyne.

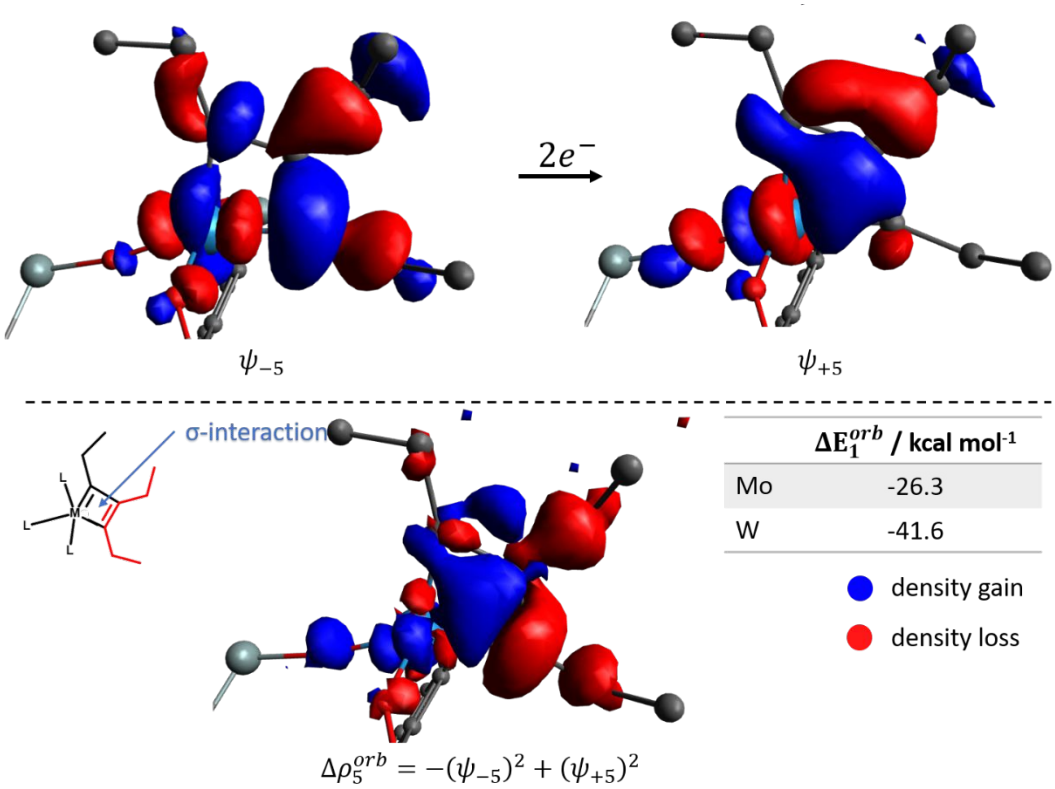

Figure S15: NOCV pair $\psi_{\pm 5}$ and the resulting difference density $\Delta\rho_5^{orb}$ for the metallacyclobutadienes. Fragment A = Alkylidyne, Framgent B = Alkyne.

Local-Energy-Decomposition Analysis

To determine the dispersion energy caused by the C-H – π interaction between the ethyl- and phenyl-groups in complex **2-MTd**, we made use of the LED scheme implemented in ORCA. The data was calculated on the DLPNO-CCSD(T)/def2-TZVP level of theory using TightPNO settings. Since the interaction is intramolecular and not intermolecular, the fragments had to assigned under breaking of bonds. Figure S16 shows the assignment of the fragments. By assigning three fragments, we minimize any error due to bond-breaking and other internal dispersion effects. We only needed to consider the dispersion interaction between fragments 2 and 3, which is shown in Table S10.

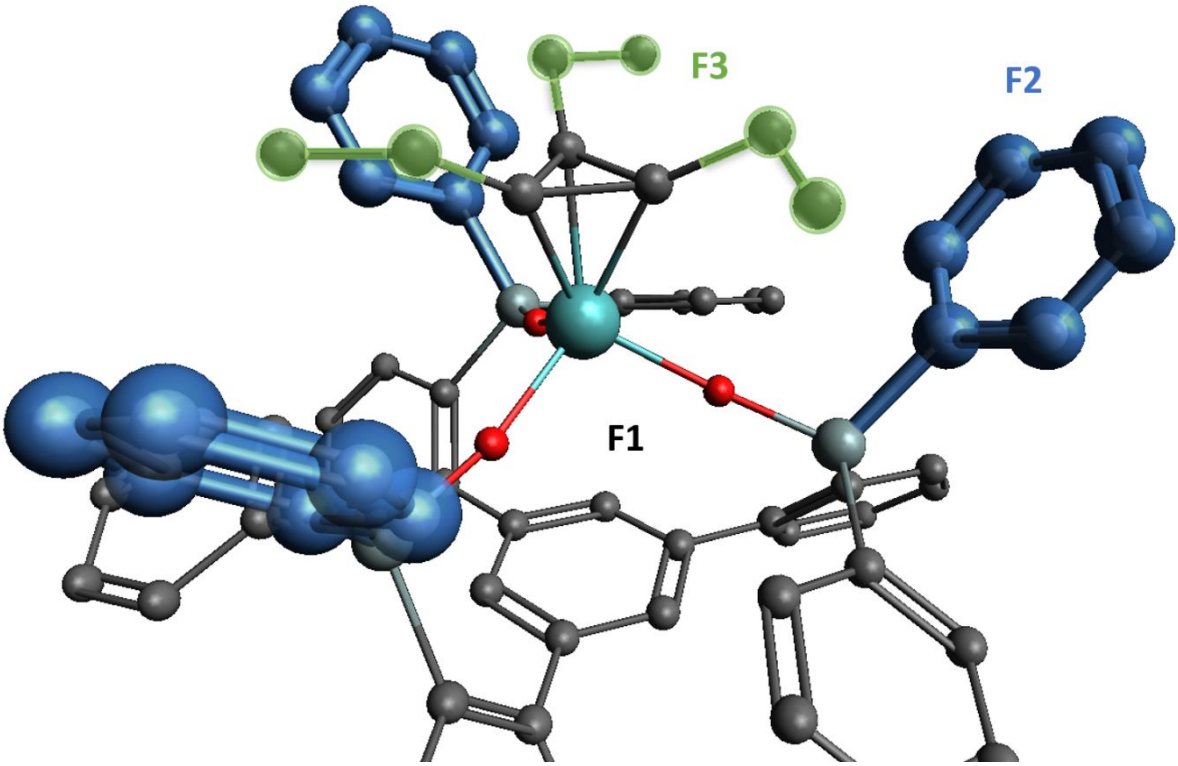

*Figure S16: Fragmentation for intramolecular LED analysis in complex **2-MTd**.*

Table S10: Dispersion interactions obtained by LED analysis on the DLPNO-CCSD(T)/def2-TZVP level of theory between fragments 2 and 3. All energied in kJ/mol.

	F2 ↔ F3
Dispersion (strong pairs)	-35.63
Dispersion (weak pairs)	-4.90
Dispersion (total)	-40.53

Spectroscopy

Details of measurement and calculation

UV-VIS measurements were performed on a Cary-6000i UV-VIS-NIR spectrometer. Resonance Raman measurements were performed on a home-built system that is based on a Trivista 555 triple monochromator. For the Gaussian deconvolution of the measured UV-VIS spectra, the amplitude A and position of each Gaussian as well as one common width σ were fitted in a least square sense to match a chosen part of the measured spectrum. Each of these Gaussians was then converted to a stick with oscillator strength f_{osc}, corresponding to the individual transitions, by:

$$f_{osc} = 1.44 \times 10^{-19} \times c \times \sqrt{2\pi\sigma^2} \times A$$

Here c is the speed of light in cm/s, the amplitude of the Gaussians A is given in L/mol/cm and the width σ is given in cm^{-1}.

In the TD-DFT calculations, only singlet states were considered. Additionally, the sticks obtained from the calculations were converted to Gaussian functions having the same width σ as experimentally determined. The sum of these Gaussians then represents the calculated envelope spectrum.

DPSS Lasers of Cobolt-Hübner have been used as monochromatic light sources. The samples were measured as free-hanging frozen droplets on a small loop at the edge of a glass pipette. Cooling to 100K is provided by a Cryostream 600 unit that uses a cold nitrogen gas stream isolated by a laminar-flow warm nitrogen stream around it to prevent condensation of moisture and also providing semi-anaerobic conditions. The scattered light was collected by a protected-silver off-axis parabolic mirror of Thorlabs and collimated onto the entrance slit of the monochromator by a quartz lense. Data have been post-processed by removing cosmic spikes, which result from cosmic particles reaching the CCD detector. They were identified by measuring up to 30 spectra without averaging them. Since the cosmic spikes are singular events, they only appear in one of these spectra. After all spikes were removed, the spectra were averaged. For every solution measured, a measurement of the pure solvent was conducted using the same settings. Both solution and solvent spectra were baseline corrected using the IALS method:

Used IALS code (written for Python 3)

```
import numpy as np
from scipy import sparse
from scipy.sparse.linalg import spsolve

def baseline_ials(xy, lam, lam1, p, plot=True):
      # S. He, W. Zhang, L. Liu, Y. Huang, J. He, W. Xie, P. Wu, and C. Du,
Anal. Methods 6, 4402 (2014).
      # code idea from https://stackoverflow.com/questions/29156532/python-
baseline-correction-library
      '''xy is a Nx2 array with the spectrum data, 10^2<lam<10^6, lam1<10^-
4 (smoothness param) and p the asymmetry param (p<0.1). Returns the
baseline corrected data in the same shape as xy is given.'''
      y = xy[:,1]
      L = len(y)
      D = sparse.diags([1,-2,1],[0,-1,-2], shape=(L,L-2))
      D1 = sparse.diags([1,-1],[0,-1], shape=(L,L-1))
      w = np.ones(L)
      w0 = np.ones(L)*2.
```

```
wthresh = 1e-4
count = 0
while np.linalg.norm((w-w0)/w0) > wthresh: # RMS threshold
      count += 1
      w0 = np.copy(w) # safe "old" w
      W = sparse.spdiags(w, 0, L, L)
      Z = W.dot(W.transpose()) + lam1*D1.dot(D1.transpose()) +
lam*D.dot(D.transpose())
      Z1 = W.dot(W.transpose()) + lam1*D1.dot(D1.transpose())
      z = spsolve(Z, Z1.dot(y))
      w = p * (y > z) + (1-p) * (y < z)
      if count > 100: break
return np.vstack([xy[:,0],z]).T
```

Then, the solution and solvent spectra were calibrated by assigning the most intense solvent peaks to their known position (from previously recorded reference spectra) and fitting these data by a second-order polynomial. After normalizing both spectra, they were subtracted and common artifacts (caused by non-optimal overlap of solvent peaks) were removed.

To simulate Resonance-Raman spectra, the displacements between the potential minima of the ground and excited states – expressed in normal coordinates – are needed. The ground state minimum is known from the geometry optimization shown above. To estimate the equilibrium of the excited states, first, the vertical excitation energy and the gradient of the excited states PES are obtained using the above mentioned TDDFT calculations on the B3LYP-D3(BJ)/def2-TZVP level of theory. Second, the Hessian of the excited state is needed. To save computation time, we approximate it by the ground state Hessian, already obtained at the TPSS-D3(BJ)/def2-TZVP level of theory. Knowing the gradient and Hessian, an extrapolation can be performed which yields an estimate of the position of the excited state minimum. The obtained displacements (in dimensionless normal coordinates) were then used in the ORCA_ASA program to simulate the Resonance-Raman intensities of each vibrational mode upon a chosen excitation. The excitation energies were manually shifted according to the difference between the respective sticks in the UV-VIS-NIR measurements. This way, the excitation energy within the Resonance-Raman calculations has the same difference to the TDDFT transition energy as the laser excitation has to the UV-VIS-NIR transition in the experiment.

Additional UV-VIS spectra

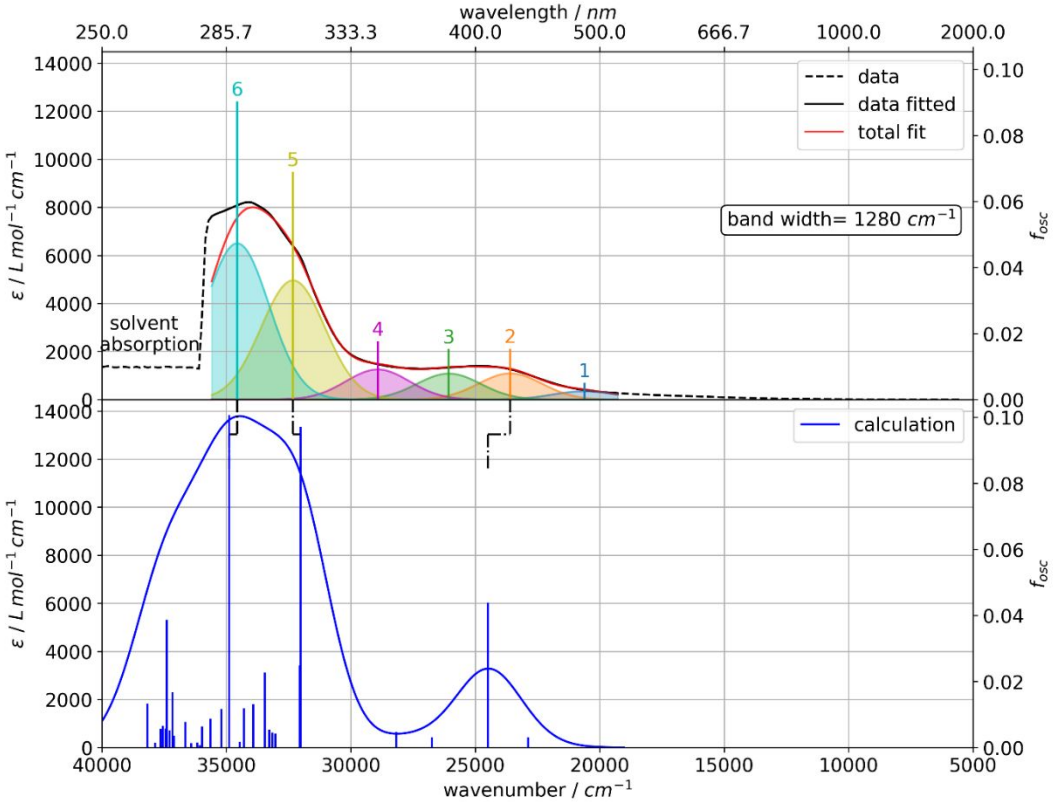

*Figure S17: Measured and calculated UV-VIS-NIR spectra of **1-CAr**. The measurement was conducted with 1mM solution in toluene at room temperature. For the TDDFT calculation, the first 30 singlet states were considered.*

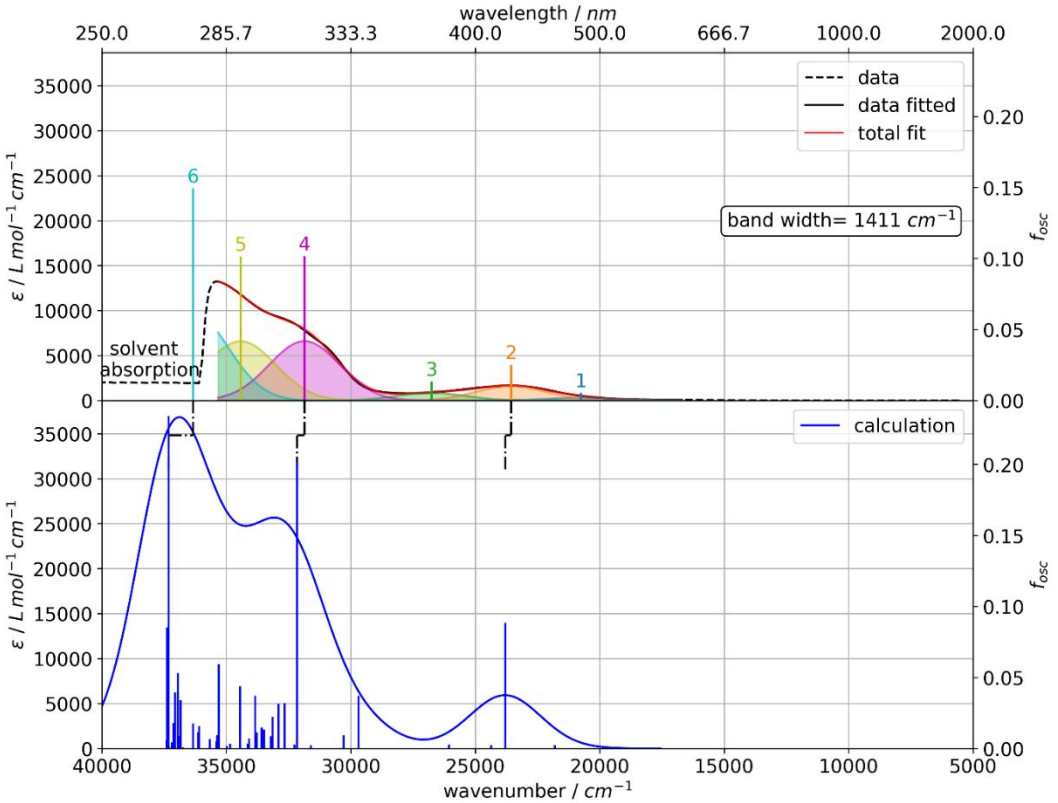

*Figure S18: Measured and calculated UV-VIS-NIR spectra of **2-CAr**. The measurement was conducted with 1mM solution in toluene at room temperature. For the TDDFT calculation, the first 40 singlet states were considered.*

Additional Resonance Raman spectra

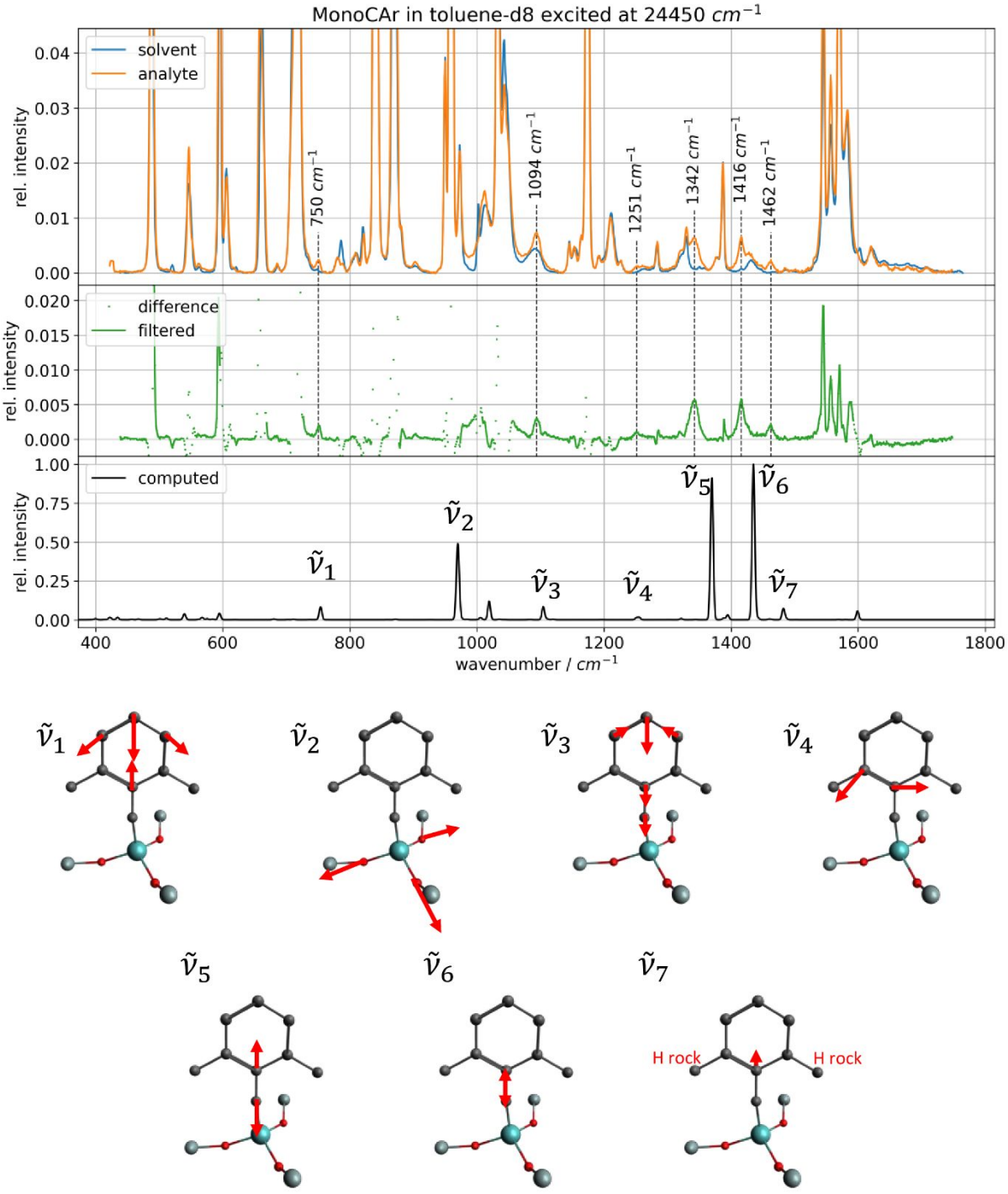

*Figure S19: Resonance-Raman spectra of the **1-CAr** complex (3 mM in toluene-d_8) at 100 K. An excitation laser with a photon energy of* $24450\ \mathrm{cm}^{-1}$ *was used at a power of 45 mW*

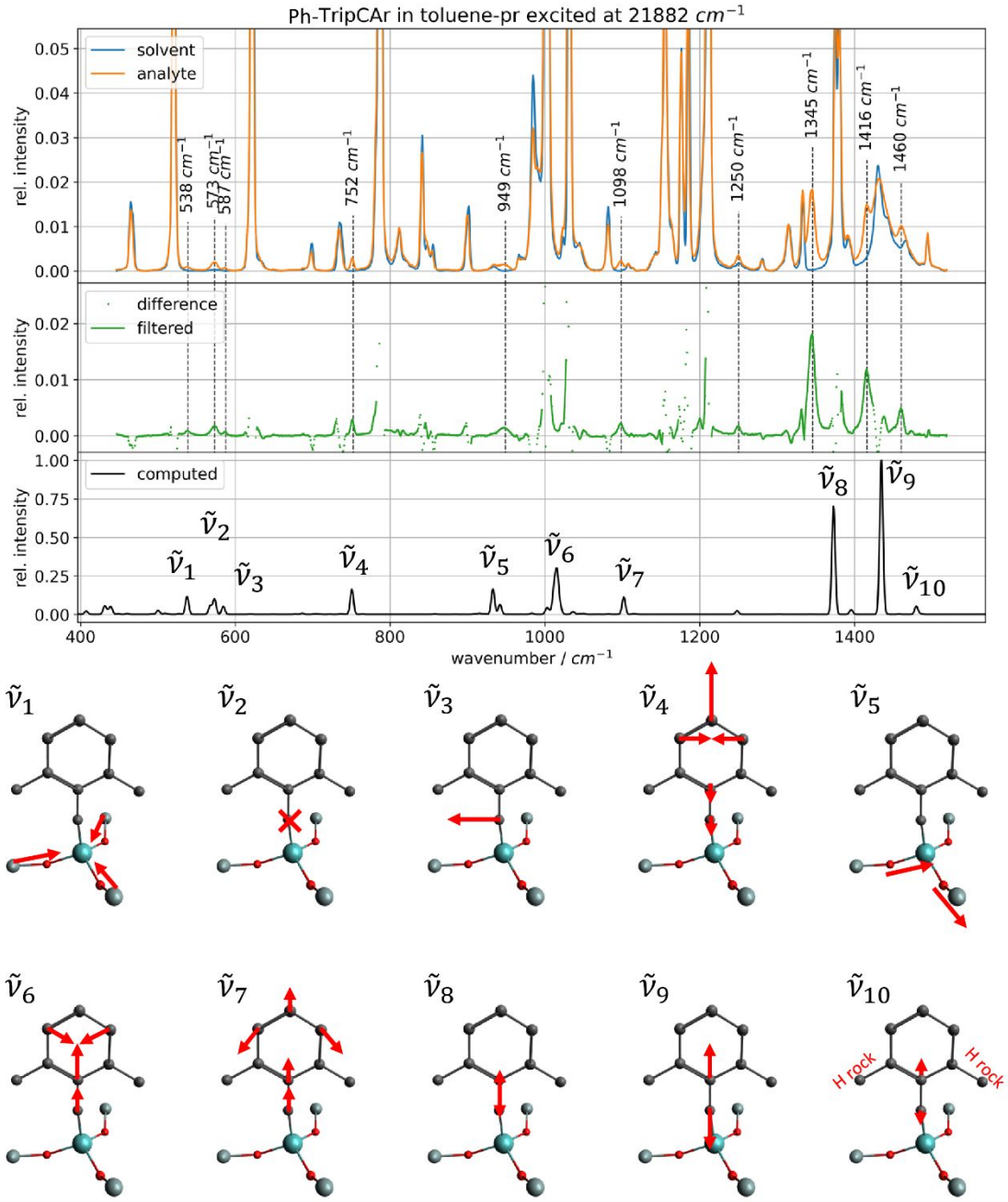

*Figure S20: Resonance-Raman spectra of the **2-CAr** complex (3 mM in toluene) at 100 K. An excitation laser with a photon energy of* $21882\ \mathrm{cm}^{-1}$ *was used at a power of 50 mW*

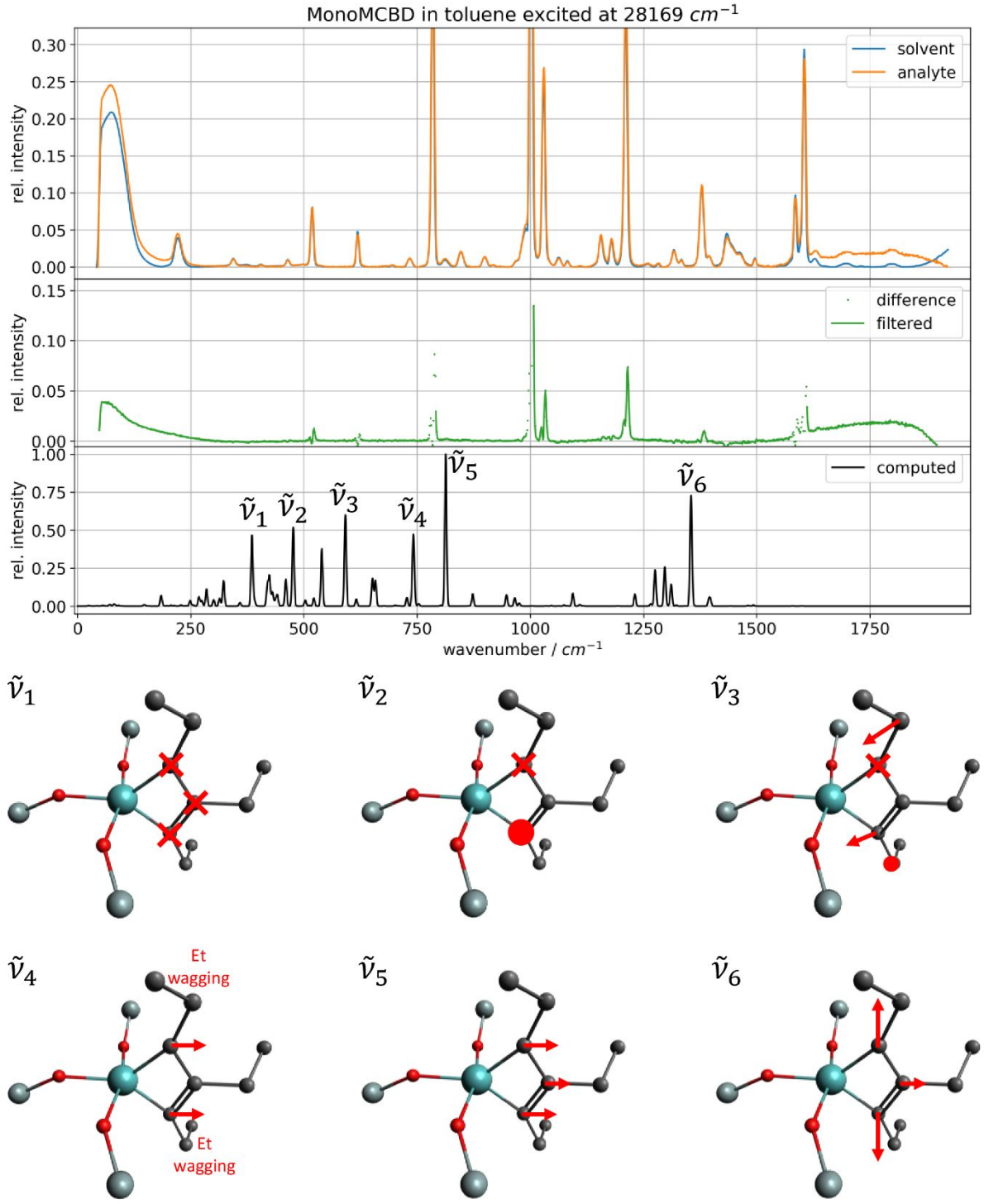

*Figure S21: Resonance-Raman spectra of intermediate **1-MCBD** (0.3 mM in toluene) at 100 K. An excitation laser with a photon energy of* $28169\ \mathrm{cm}^{-1}$ *was used at a power of 20 mW. Higher concentrations gave strong fluorescence, especially when irradiating the solid crystals of **1-MCBD** directly.*

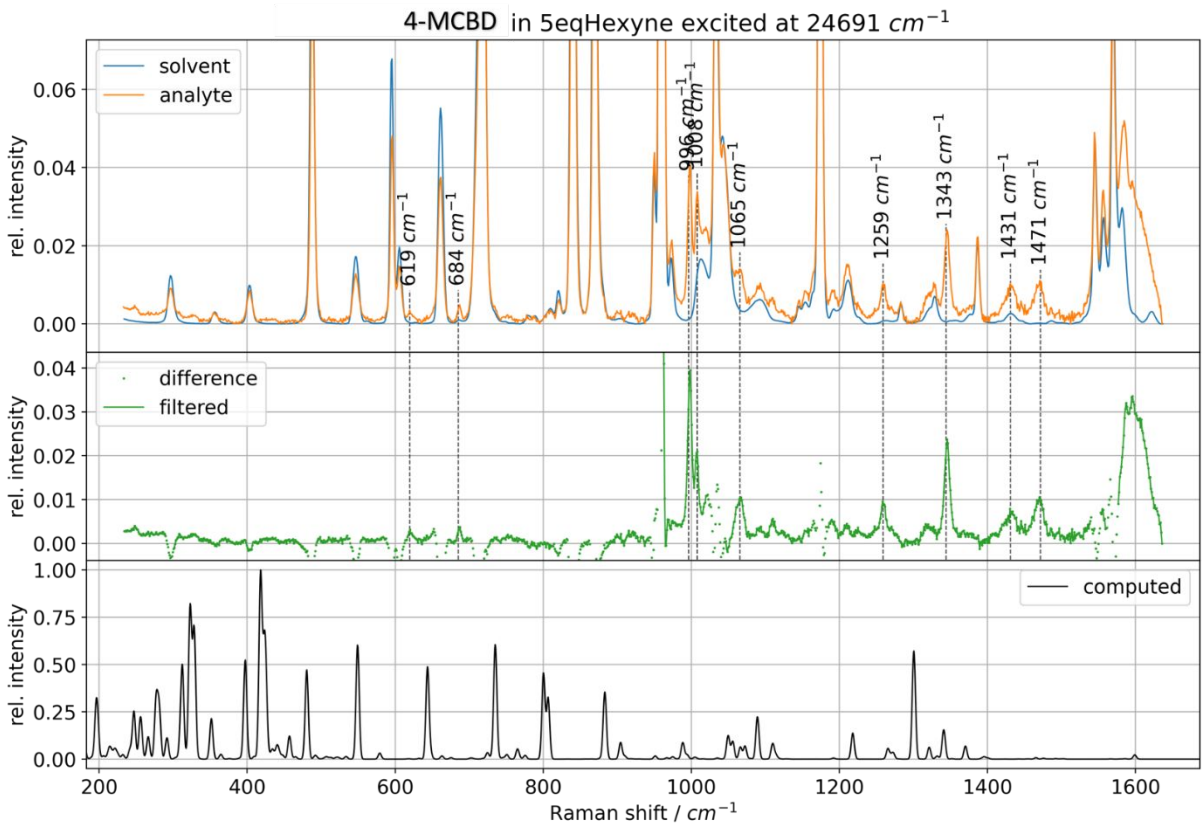

*Figure S22: Resonance-Raman spectra of intermediate **4-MCBD** (48 mM in toluene) at 100 K. An excitation laser with a photon energy of* $24691\ \mathrm{cm}^{-1}$ *was used at a power of 10 mW.*

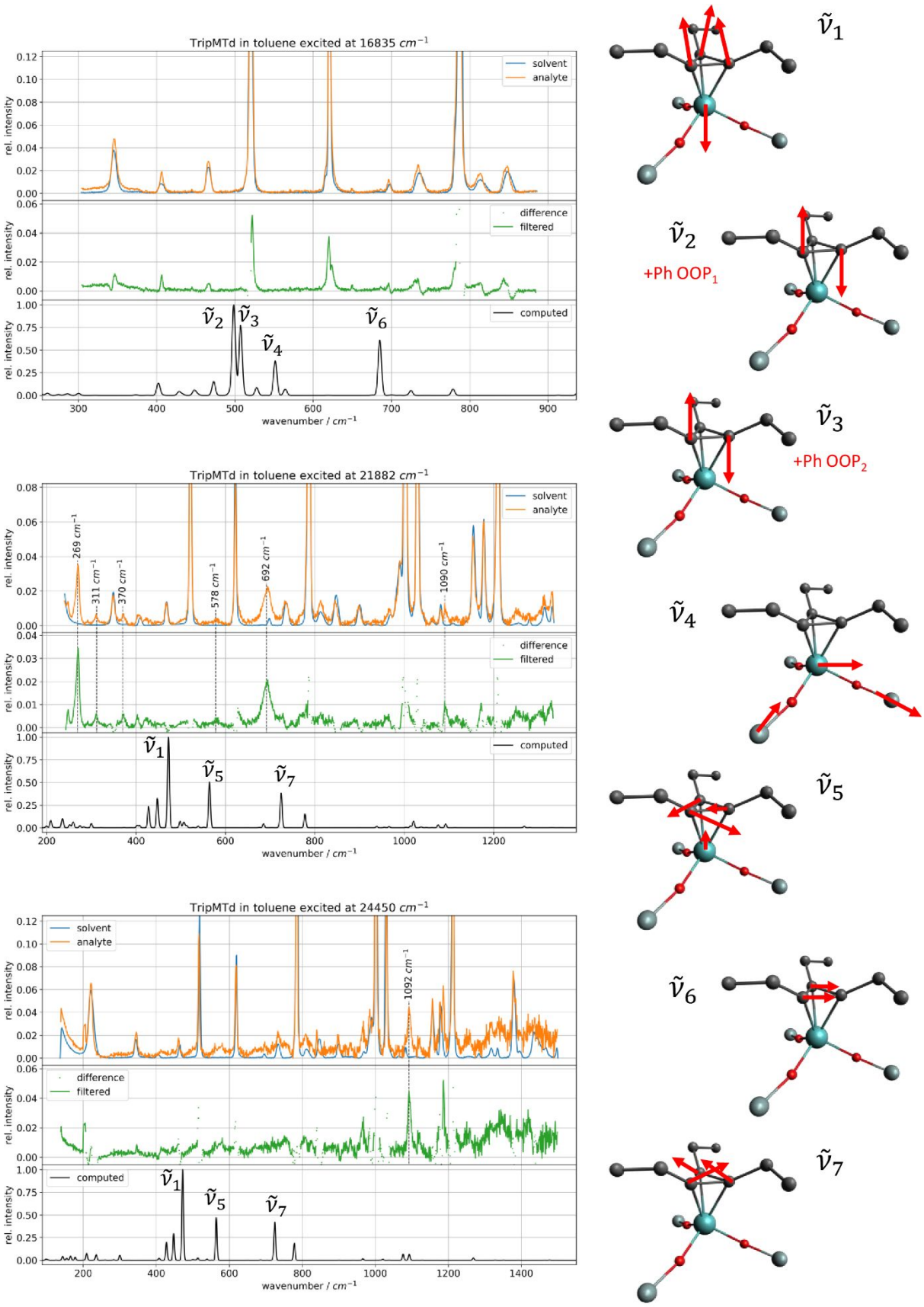

*Figure S23: Resonance-Raman spectra of intermediate **2-MTd** (20 mM in toluene) at 100 K. Excitation lasers with photon energies of* $16835\ \mathrm{cm}^{-1}$, $21882\ \mathrm{cm}^{-1}$ *and* $24450\ \mathrm{cm}^{-1}$ *were used, each at a power of 20 mW.* $\tilde{\nu}_1$, $\tilde{\nu}_5$ *and* $\tilde{\nu}_7$ *describe different twisting motions of the* C_3*-unit while moving up or down, relative to the molybdenum atom. OOP=out-of-plane*

Difference densities of intermediate complexes

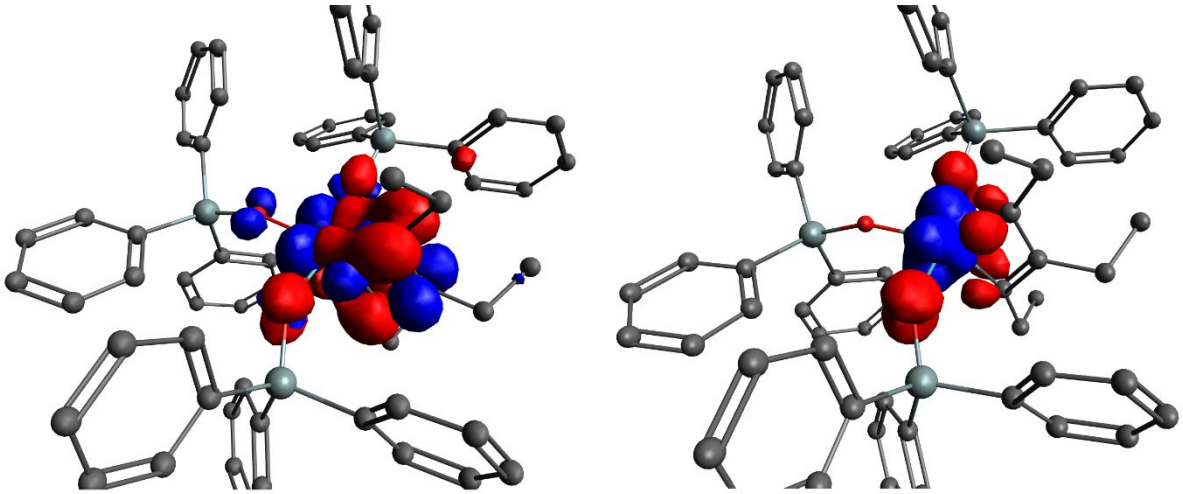

Figure S24: Difference densites of the calculated transitions 1 and 4 at $17482\ cm^{-1}$ *and* $31214\ cm^{-1}$ *respectively, of the* ***1-MCBD****. Blue corresponds to a gain in electron density while red represents a loss. Isosurface at 0.003.*

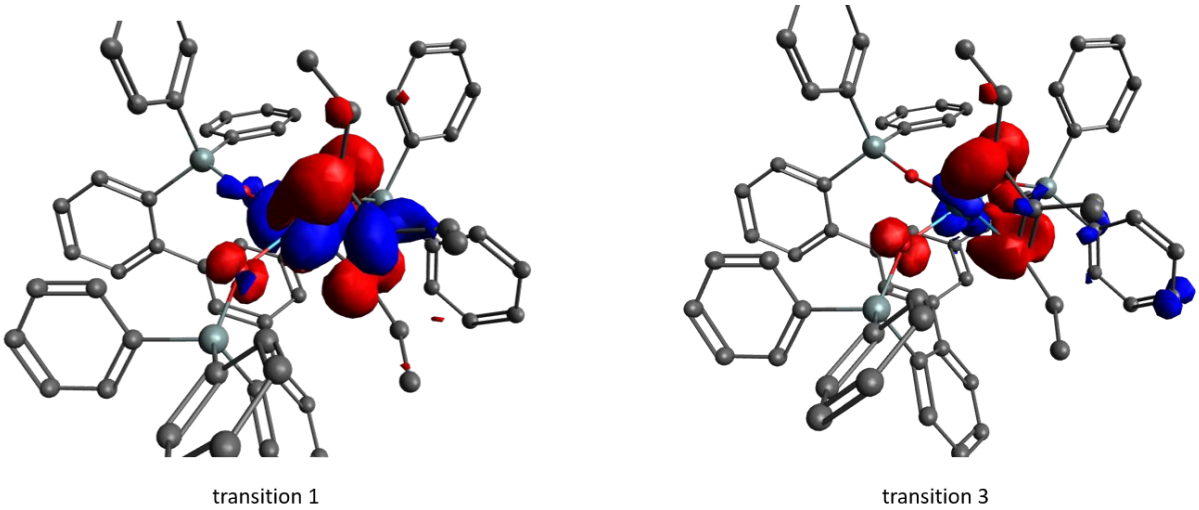

Figure S25: Difference densites of the calculated transitions 1 and 3 at $19259\ cm^{-1}$ *and* $30362\ cm^{-1}$ *respectively, of the* ***4-MCBD****. Blue corresponds to a gain in electron density while red represents a loss. Isosurface at 0.003.*

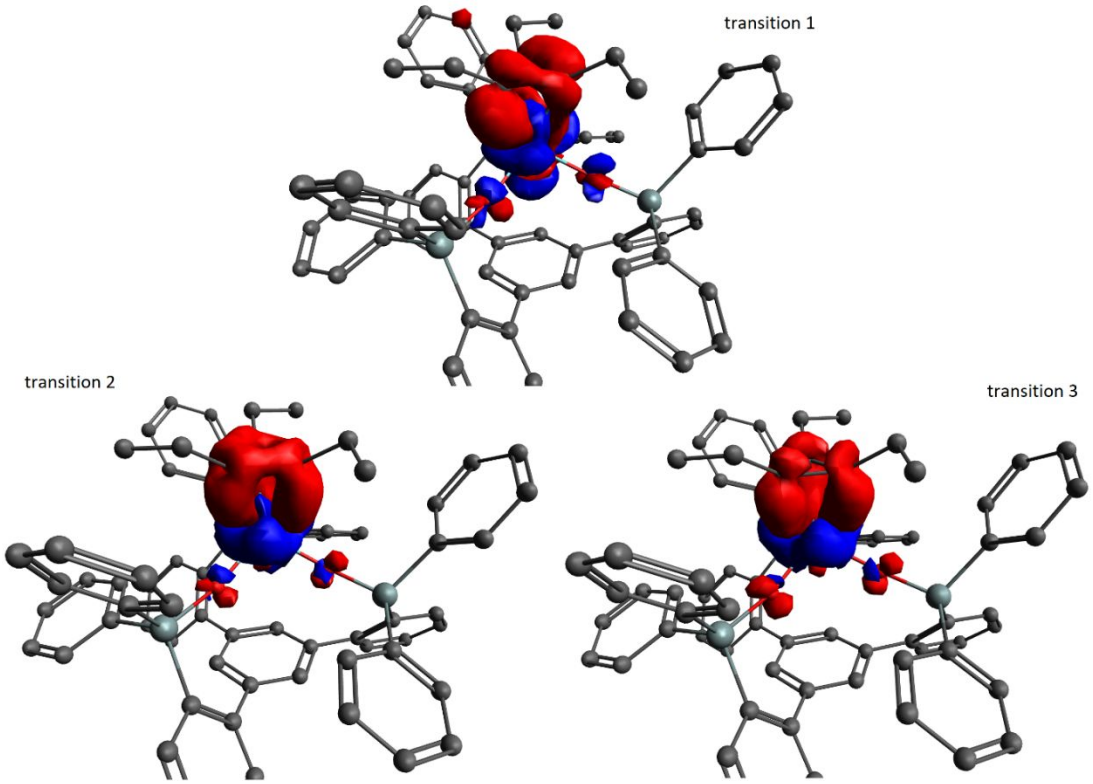

Figure S26: Difference densties of the calculated transitions 1-3 at $19650\ cm^{-1}$, $22660\ cm^{-1}$ *and* $25918\ cm^{-1}$, *respectively, of the* ***2-MTd*** *complex. Blue corresponds to a gain in electron density while red represents a loss. Isosurface at 0.003.*

NMR comparison

For further comparison of the electronic structure from experiment and calculation, ^{1}H- and ^{13}C-NMR spectra were measured (see EXPERIMENTAL NMR-SPECTRA below) and computed. For the calculations, again the B3LYP-D3BJ functional (and dispersion correction) were used. We increased the basis set to def2-TZVPP and also increased the grid size for the RIJCOSX approximation. To transform the calculated NMR shieldings into chemical shifts, an external or internal reference is needed. We chose to always use an internal reference, mostly an alkyl group with small chemical shifts. Since the ^{13}C-NMR spectra are of more interest with respect to the electronic structure of the core complexes, we will restrict our discussion on these data.

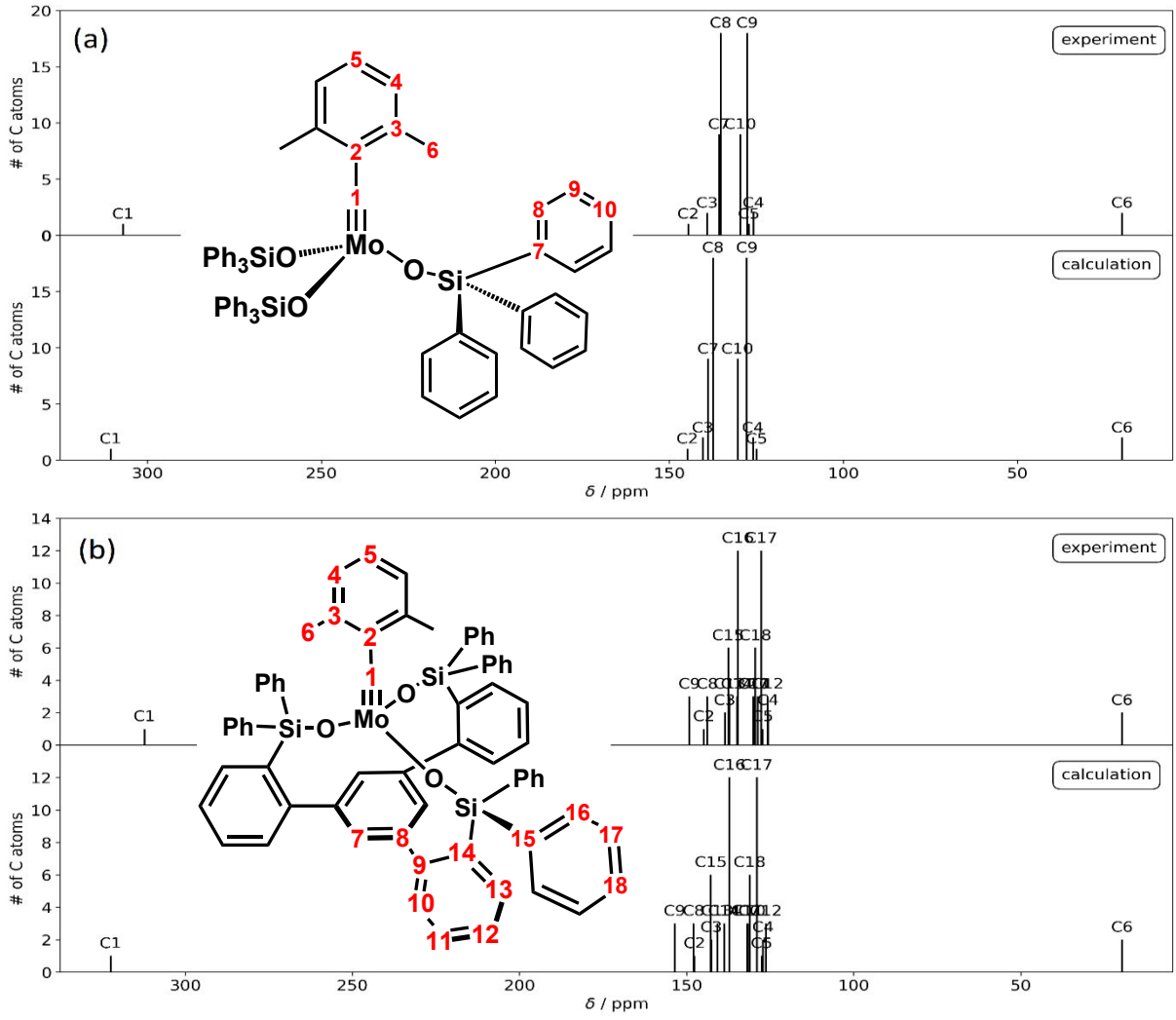

*Figure S27: Experimental and calculated ^{13}C shifts (no fine structure) of (a) the **1-CAr** and (b) the **2-CAr** complex. For both calculations C6 was used as internal reference.*

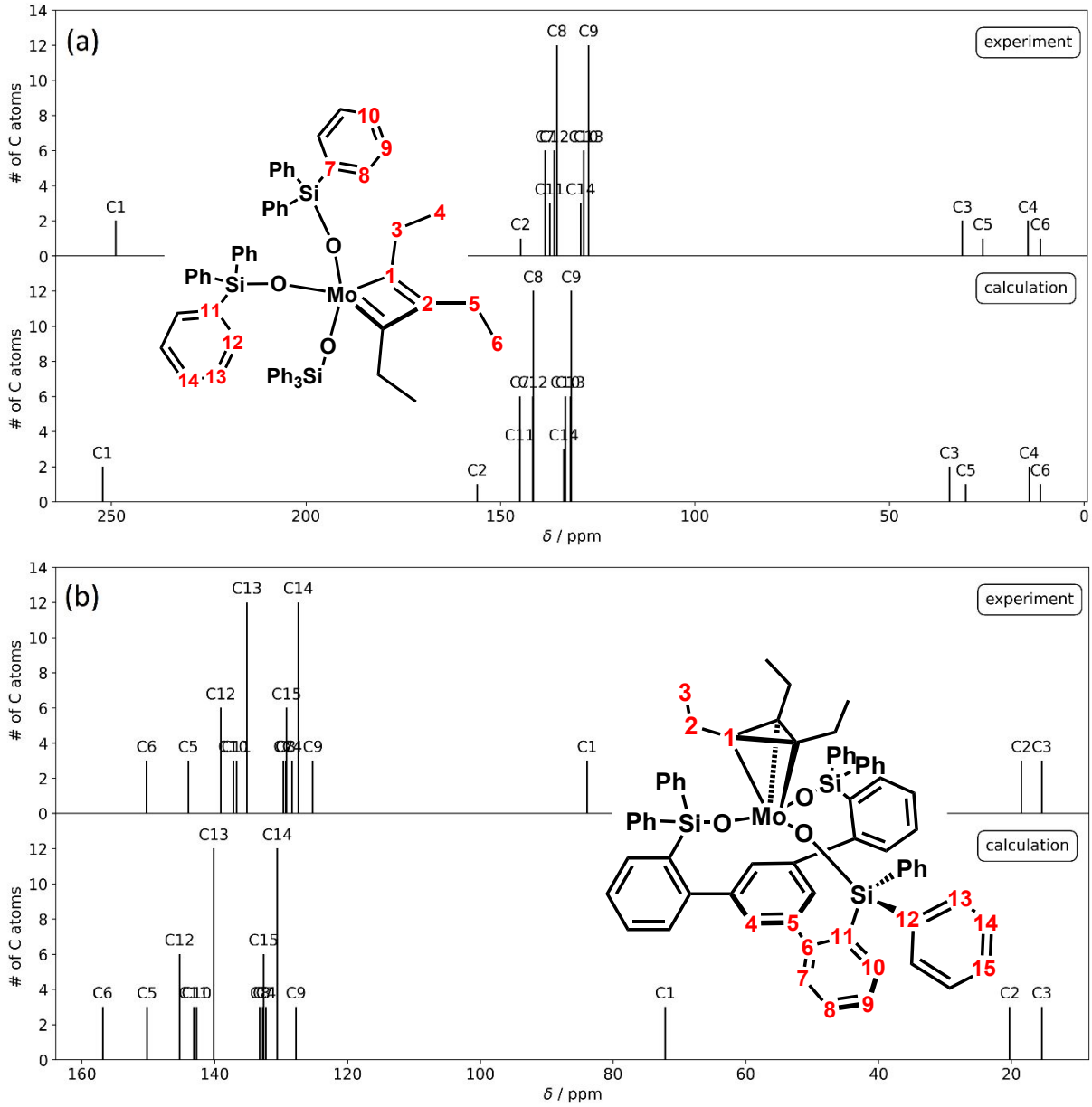

*Figure S28: Experimental and calculated ^{13}C shifts (no fine structure) of (a) the **1-MCBD** complex and (b) the **2-MTd** complex. For the calculations C6 and C3, respectively, were used as internal reference.*

Kinetic Modeling

Nudged-Elastic-Band calculations

The NEB method yields a number of structures (images), that connect two minima via a smooth transition. We normally choose 16 images. These form the minimum energy path (MEP). We always performed climbing image NEB (NEB-CI) calculation in which the highest energy image (HEI) is pushed uphill along the path tangent. This way, a very good approximation to the actual transition state (TS), which lies on the MEP, is obtained, especially since we used rather tight convergence criteria for the CIs. Hessians calculated at the CIs always revealed the TS mode with the largest imaginary frequency and only few low-lying imaginary frequencies were obtained alongside. The CIs together with their Hessians were used for a subsequent TS search. Unfortunately, especially for the association reactions, these TS optimizations often failed due to the complex structure of the PES caused by many internal rotations and soft vibrations of the complexes. We thus often had to use the CI and its Hessian as an approximation to the TSs. We are confident that this only introduces small errors since the energy differences between CIs and TSs (in those cases, where they were found) were below 5 kJ/mol.

Rate constant estimation using Eyring

Using the Eyring theory, the rate constant k of a unimolecular reaction can be estimated from the difference of the Gibbs free energy of the reactant and the corresponding transition state, $\Delta G^{\ddagger}$, by:

$$k(T) = \kappa \frac{k_B T}{h} \exp\left(-\frac{\Delta G^{\ddagger}}{RT}\right)$$

where κ is the transition coefficient (we assume 0.5), k_B is the Boltzmann constant, h is Planck's constant, T is the absolute temperature and R is the ideal gas constant (since $\Delta G^{\ddagger}$ is applied as molar quantity).

If the equilibrium constant K between two stable minima is needed, the forward and backward reaction rates, k_f and k_b, respectively, can be used:

$$K = \frac{k_f}{k_b} = \exp\left(-\frac{\Delta G}{RT}\right)$$

where ΔG is the difference of Gibbs free energy of the two minima. Here we assumed $\kappa_f = \kappa_b$, thus cancelling the whole pre-exponential factor in the ratio of the rate constants.

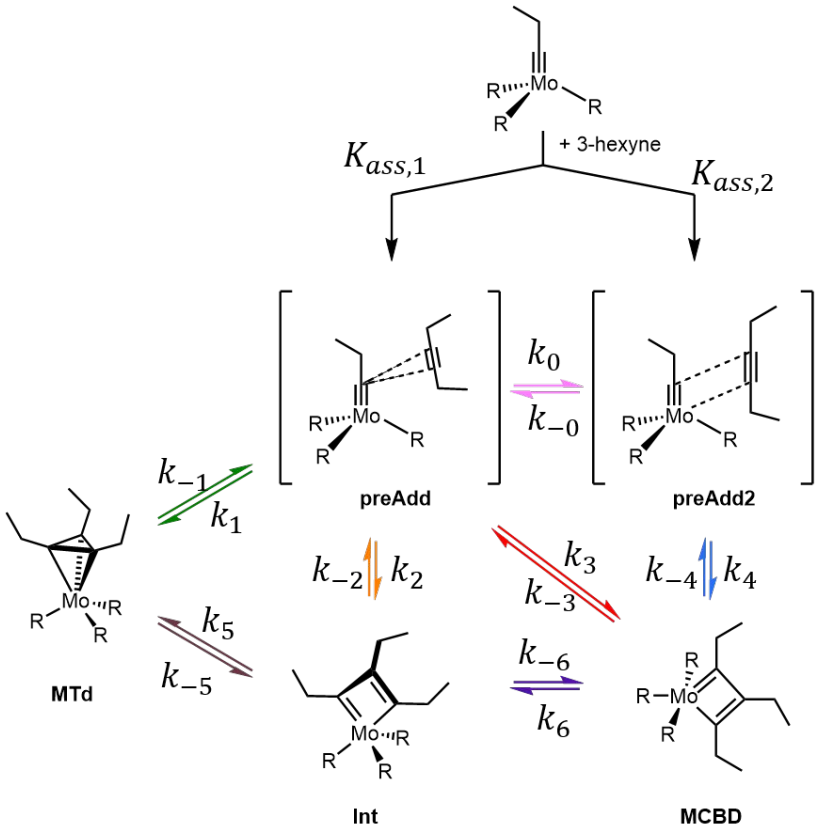

Figure S29: Full Reaction System with all rate constants.

Temporal evolution

To model the temporal evolution of our reaction system, we made a few simplifications. I.e., we never explicitly considered the population of the pre-adduct complexes but only modeled the dissociated state (“diss”) and the three stable intermediates.

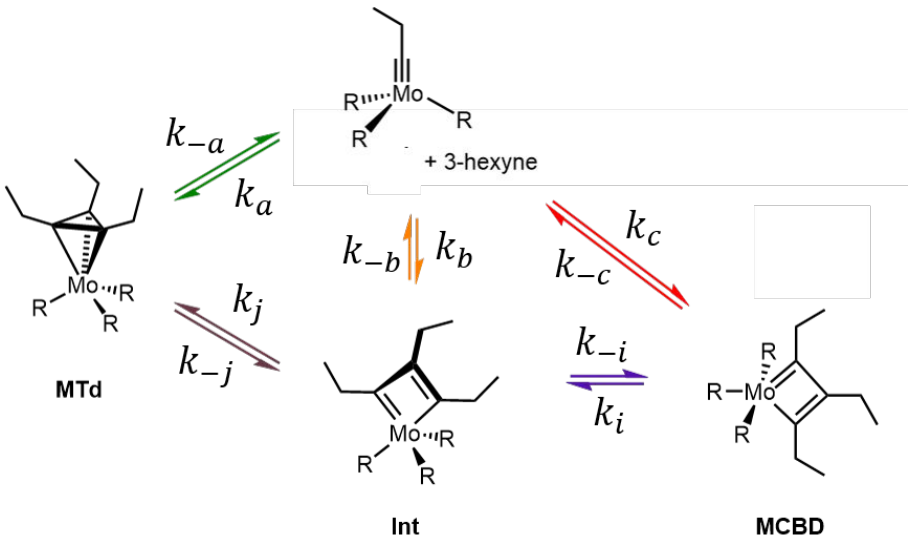

Figure S30: Simplified Reaction System with rate constants.

Thus, the system at a point in time t can be described by a vector of concentrations

$$\boldsymbol{x}(t) = \begin{pmatrix} [diss] \\ [MTd] \\ [Int] \\ [MCBD] \end{pmatrix}.$$

Formulating all rate equations for this system is fairly easy and can also be written in matrix form:

$$\dot{\boldsymbol{x}}(t) = \boldsymbol{k} \cdot \boldsymbol{x}(t) = \begin{pmatrix} -(k_a + k_b + k_c) & k_{-a} & k_{-b} & k_{-c} \\ k_a & -(k_{-a} + k_{-j}) & k_j & 0 \\ k_b & k_{-j} & -(k_j + k_{-b} + k_{-i}) & k_i \\ k_c & 0 & k_{-i} & -(k_{-c} + k_i) \end{pmatrix} \cdot \boldsymbol{x}(t)$$

where $\dot{\boldsymbol{x}}(t)$ is the temporal derivative of the state vector and we call $\boldsymbol{k}$ the rate matrix.

To obtain the rate constants for the simplified system from those of the full system, we made the assumption that the equilibration between the dissociated state and the pre-adduct complexes is always fast. Thus, the formation of e.g., MTd from diss can be described by $[alkyne] \times K_{ass,1} \times k_1$. We used slightly different models for **2** and **3** with respect to preAdd2. For **2**, we assumed that $k_0 \gg k_4$. For **3**, we treated both pre-adduct complexes the same. We thus used the following two reaction systems

Reactant	Product	Name of rate constant	Composition in **2**	Composition in **3**
Diss	MTd	k_a	$k_1 \cdot K_{ass,1} \cdot [alkyne]$	
MTd	Diss	k_{-a}	k_{-1}	
Diss	Int	k_b	$k_2 \cdot K_{ass,1} \cdot [alkyne]$	
Int	Diss	k_{-b}	k_{-2}	
Diss	MCBD	k_c	$(k_3 + k_0) \cdot K_{ass,1} \cdot [alkyne]$	$(k_3 \cdot K_{ass,1} + k_4 \cdot K_{ass,2}) \cdot [alky$
MCBD	Diss	k_{-c}	$k_{-3} + k_0 k_4 / k_{-4}$	$k_{-3} + k_{-4}$
MCBD	Int	k_i	k_6	
Int	MCBD	k_{-i}	k_{-6}	
Int	MTd	k_j	k_5	
MTd	Int	k_{-j}	k_{-5}	

For numerical integration over time, we used state-transition theory and calculated the state-transition matrix $\boldsymbol{\phi}(\Delta t)$ using matrix exponentials.

$$\boldsymbol{\phi}(\Delta t) = \exp\left(\Delta t \cdot \boldsymbol{k}\right)$$

Δt has to be chosen small enough that the Taylor expansion of the matrix exponential still converges. We took Δt as 10% of the fastest rate in $\boldsymbol{k}$. With that, we can integrate using either of the two equations:

$$\boldsymbol{x}(t + \Delta t) = \boldsymbol{\phi}(\Delta t) \cdot \boldsymbol{x}(t)$$

$$\boldsymbol{x}(t + n \cdot \Delta t) = [\boldsymbol{\phi}(\Delta t)]^n \cdot \boldsymbol{x}(t)$$

The latter equation allows us to take timesteps $n \cdot \Delta t$, which would normally be too large for the matrix exponential. I.e., numerically $[\boldsymbol{\phi}(\Delta t)]^n \neq \boldsymbol{\phi}(n \cdot \Delta t)$, which normally should be the case.

For reference, we report the used state-transition matrices:

*Table S11: State-transition matrices of the two reaction systems (**2-CEt** + 3-hexyne and **3-CEt** + 3-hexyne). The entry ϕ_{ij} can be read as the portion of j that flows into i within the given time step through all channels.*

to\from	2-CEt	2-MTd	2-Int	2-MCBD	3-CEt	3-MTd	3-Int	3-MCBD
X-CEt	1.00E+00	4.11E-19	9.31E-10	2.95E-06	9.99E-01	2.47E-18	5.12E-06	3.26E-05
X-MTd	6.70E-13	1.00E+00	1.00E+00	1.44E-06	3.43E-19	1.00E+00	4.87E-06	9.60E-16
X-Int	1.24E-15	8.16E-13	1.24E-12	1.33E-09	1.28E-13	8.77E-13	7.04E-01	3.14E-10
X-MCBD	9.31E-07	2.79E-13	3.16E-04	1.00E+00	7.68E-04	1.63E-13	2.96E-01	1.00E+00

Time steps are: $n \cdot \Delta t(\mathbf{2}) = 10^{-7}$s and $n \cdot \Delta t(\mathbf{2}) = 10^{-13}$s

EXPERIMENTAL NMR-SPECTRA

^{1}H NMR of Complex S1, 400 MHz, C_6D_6, 25 °C

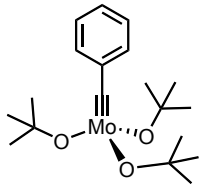

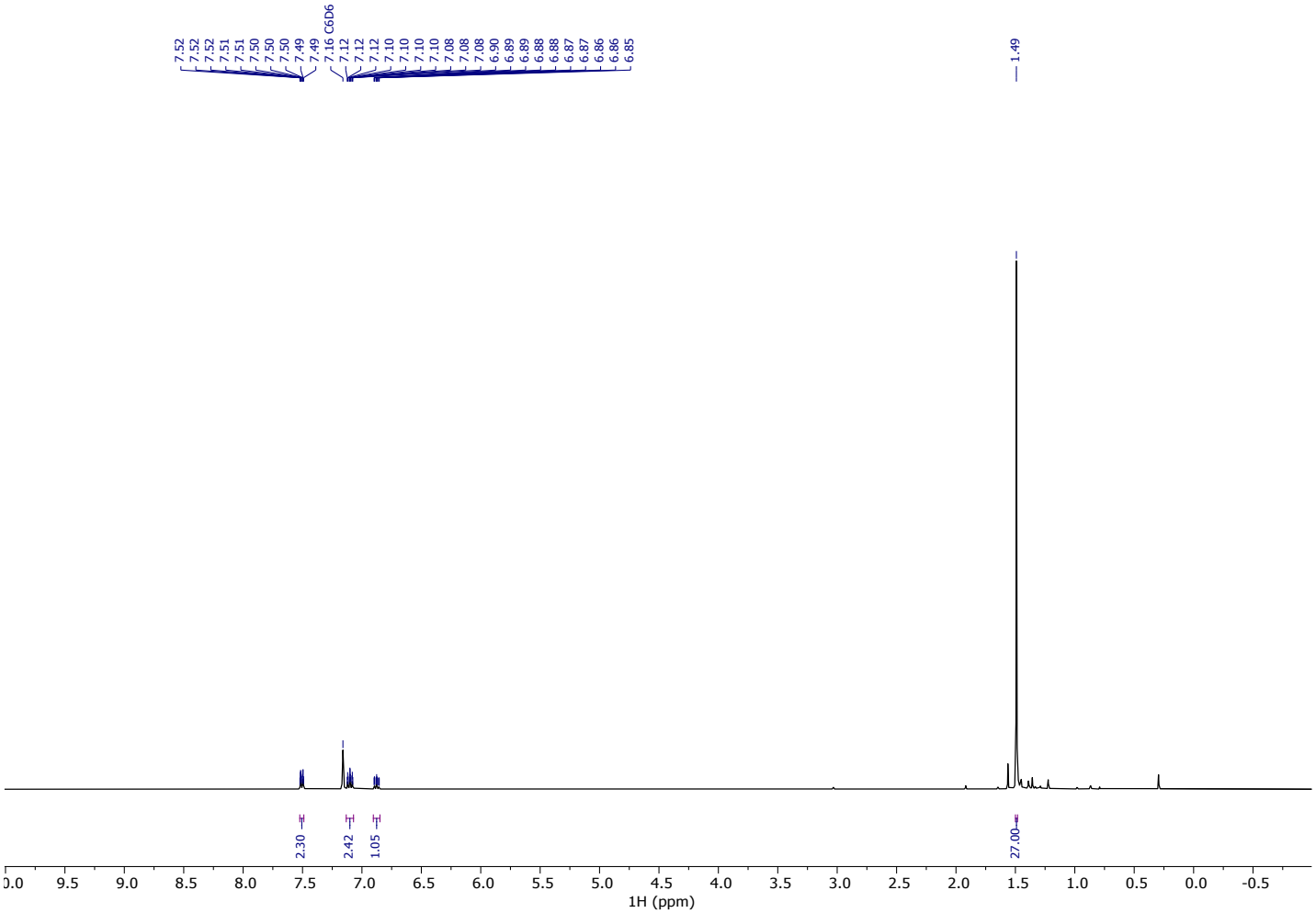

^{13}C NMR of Complex S1, 101 MHz, C_6D_6, 25 °C

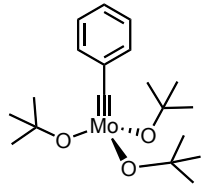

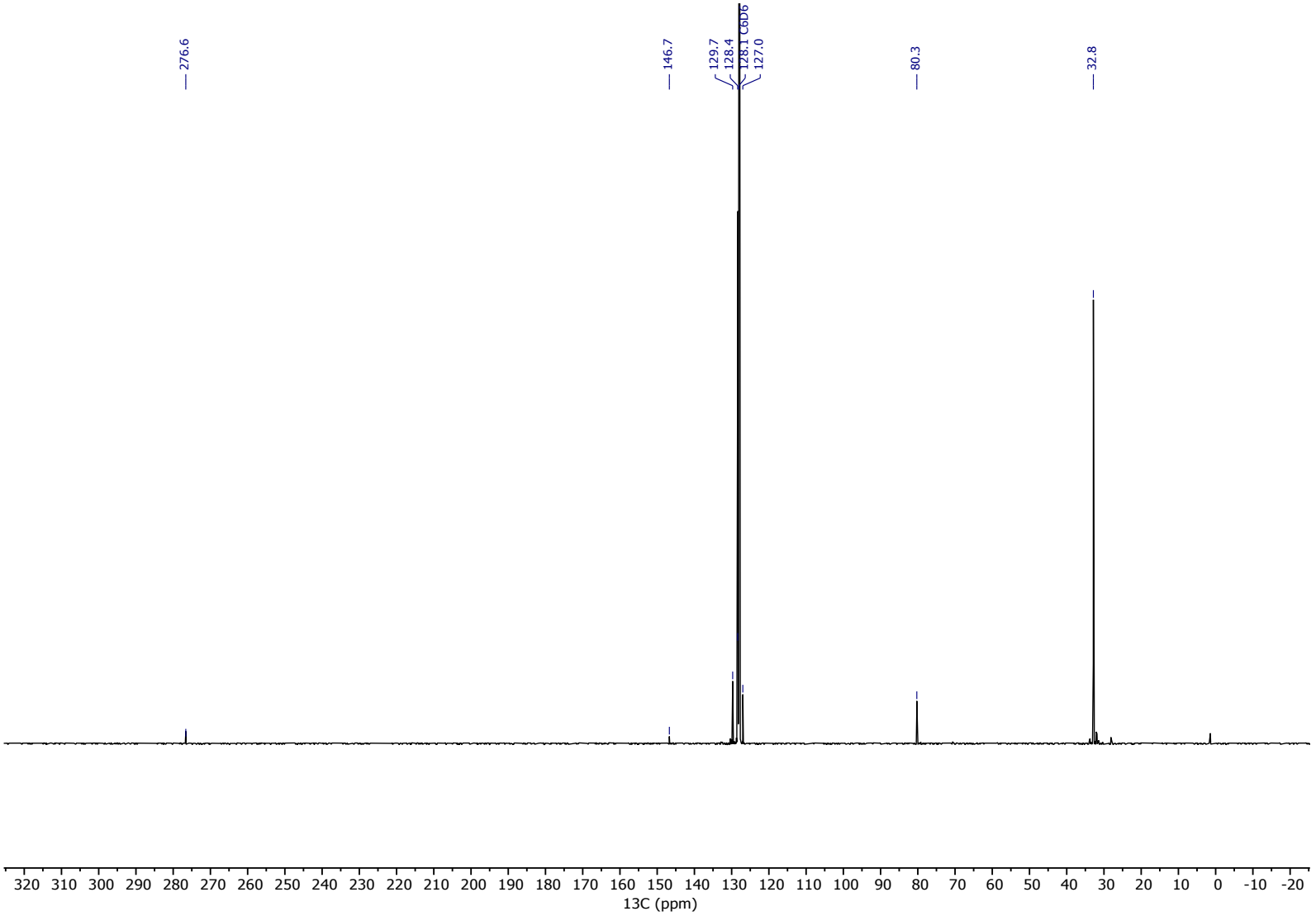

^{95}Mo NMR of Complex S1, 26 MHz, $C_6D_5CD_3$, 60 °C

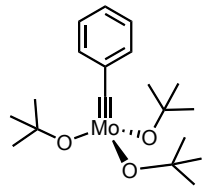

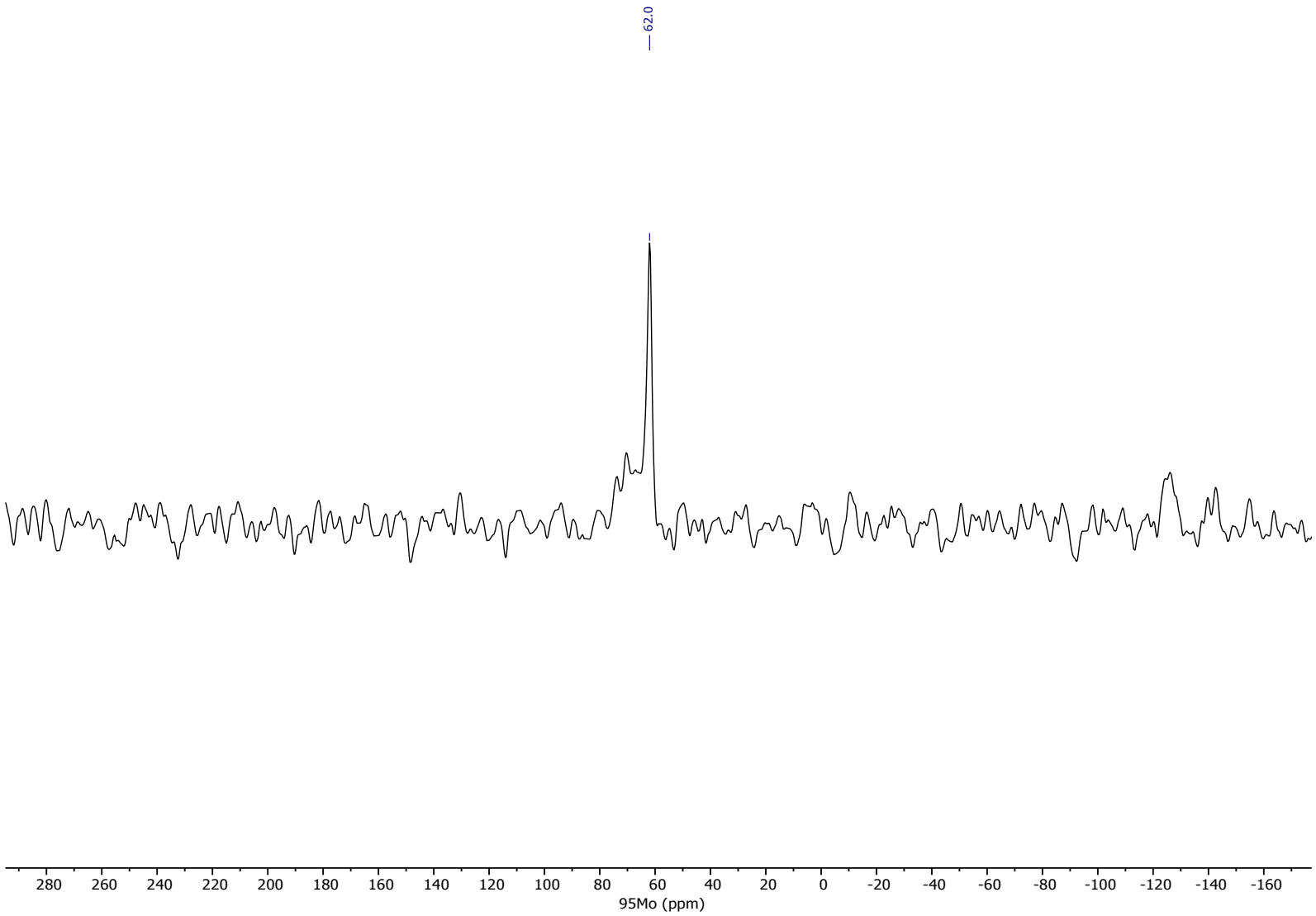

^{1}H NMR of Conversion of Complex [S3]$_2$ to S3, $C_6D_5CD_3$, 1h at 60 °C

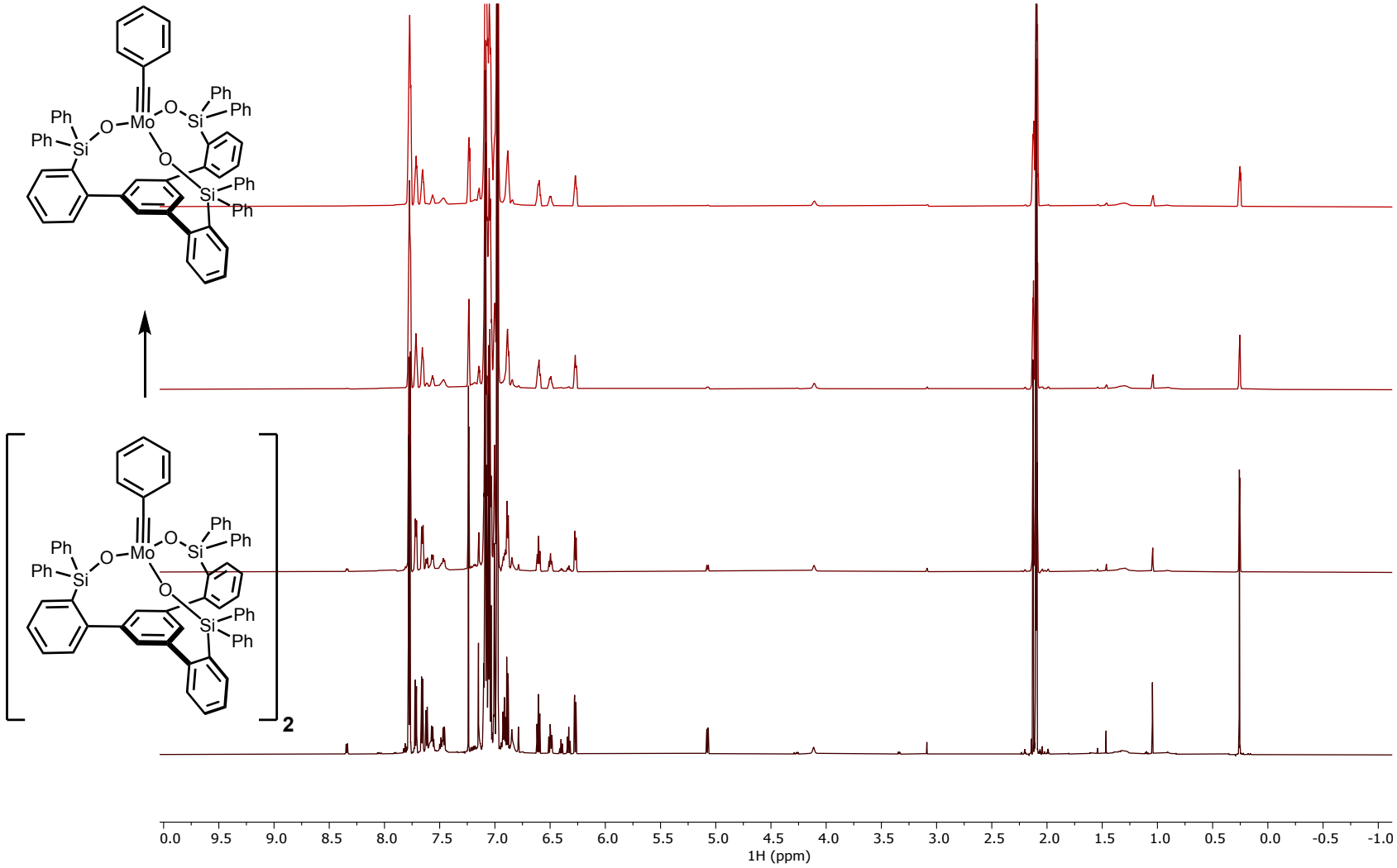
Ph
Ph
Si
O
Mo
O
Si
Ph
Ph
O
Si
Ph
Ph
2
0.0
9.5
9.0
8.5
8.0
7.5
7.0
6.5
6.0
5.5
5.0
4.5
4.0
3.5
3.0
2.5
2.0
1.5
1.0
0.5
0.0
-0.5
-1.0
1H (ppm)

^{1}H NMR of Complex S3, 600 MHz, $C_6D_5CD_3$, 25 °C

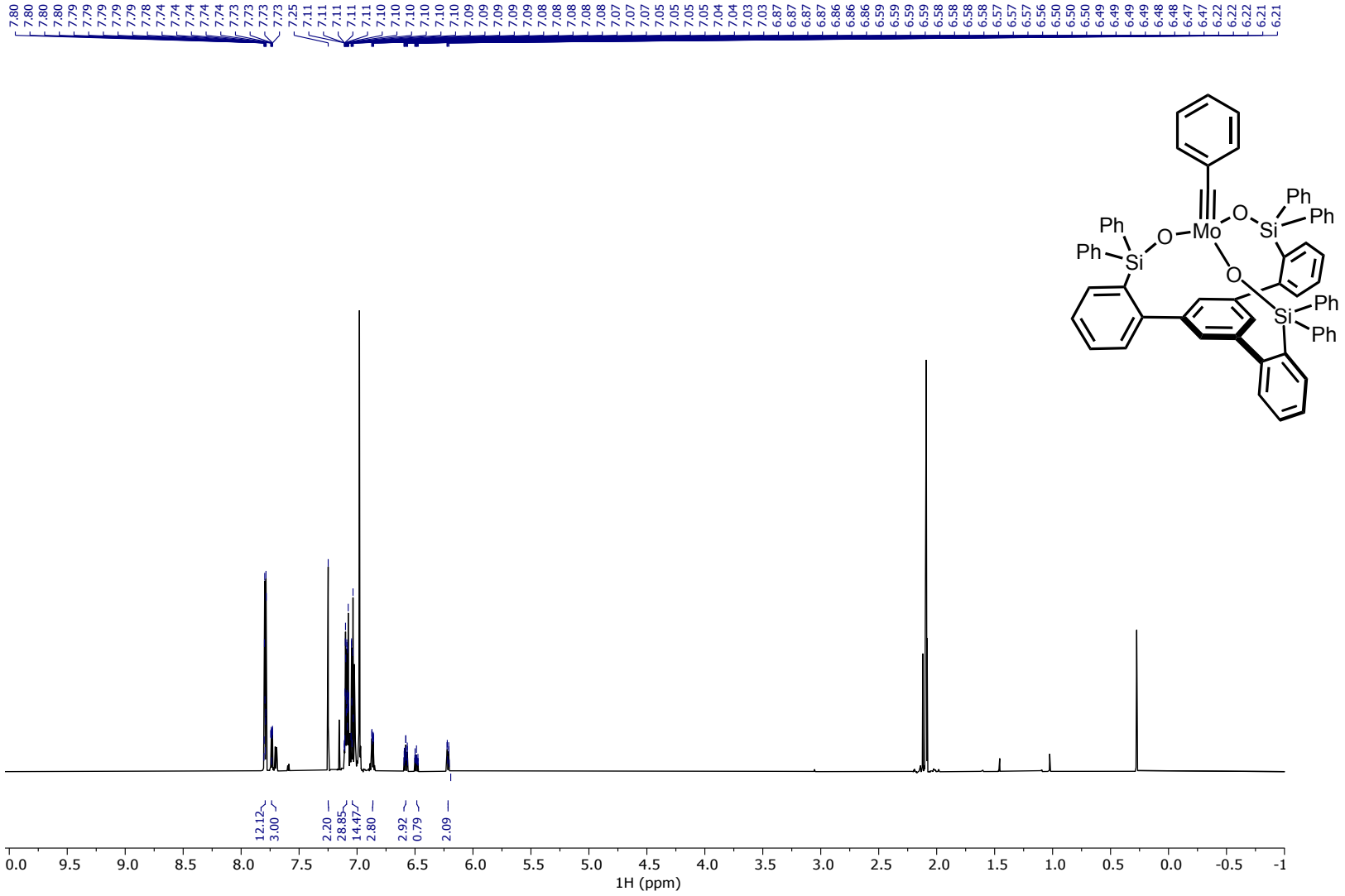

^{13}C NMR of Complex S3, 151 MHz, $C_6D_5CD_3$, 25 °C

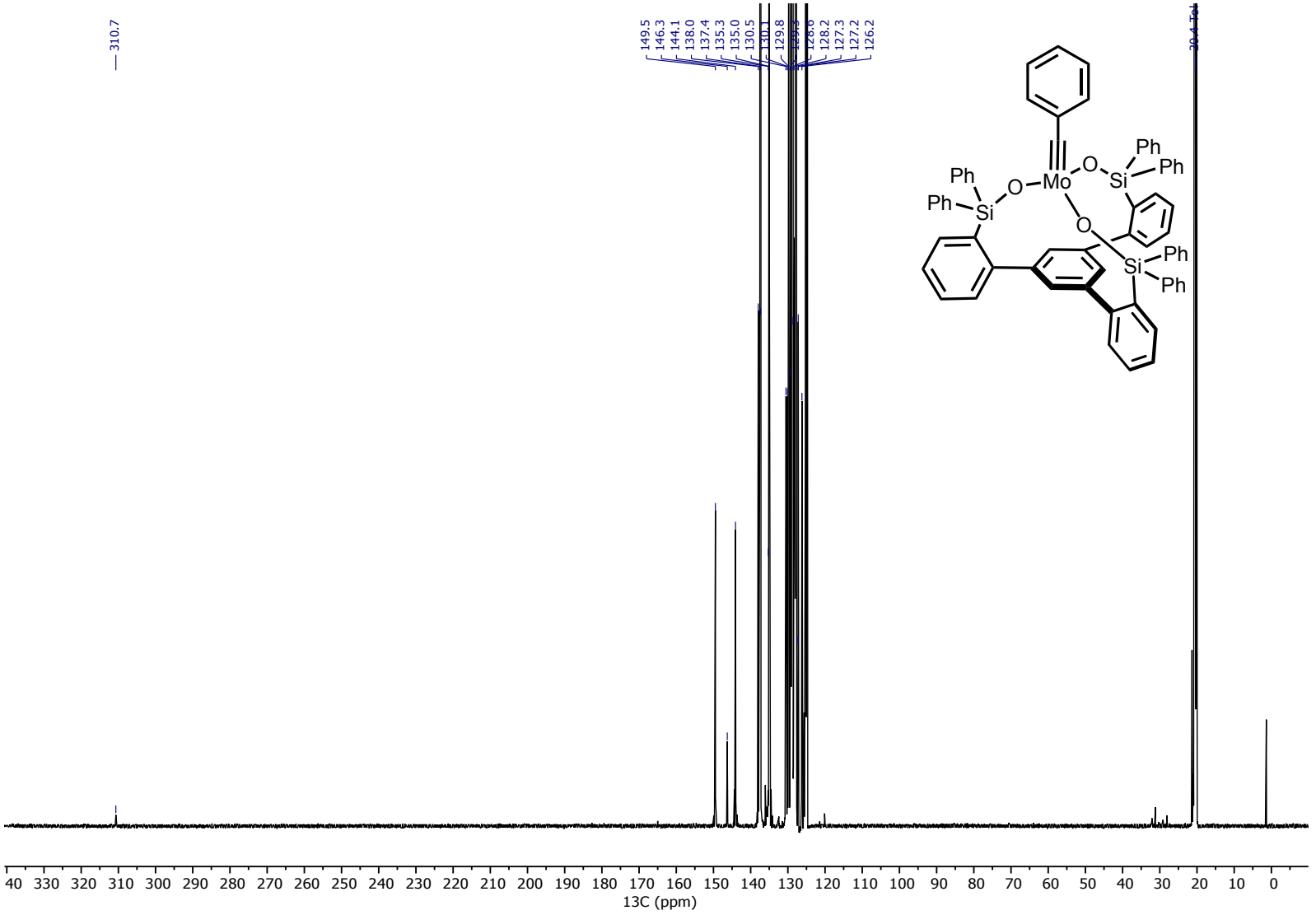
310.7
149.5
146.3
144.1
138.0
137.4
135.3
135.0
130.5
130.1
129.8
128.6
128.2
127.3
127.2
126.2
Ph
Ph
Si
O
Mo
O
Si
Ph
Ph
O
Si
Ph
Ph
40 330 320 310 300 290 280 270 260 250 240 230 220 210 200 190 180 170 160 150 140 130 120 110 100 90 80 70 60 50 40 30 20 10 0
13C (ppm)

^{29}Si NMR of Complex S3, 119 MHz, $C_6D_5CD_3$, 25 °C

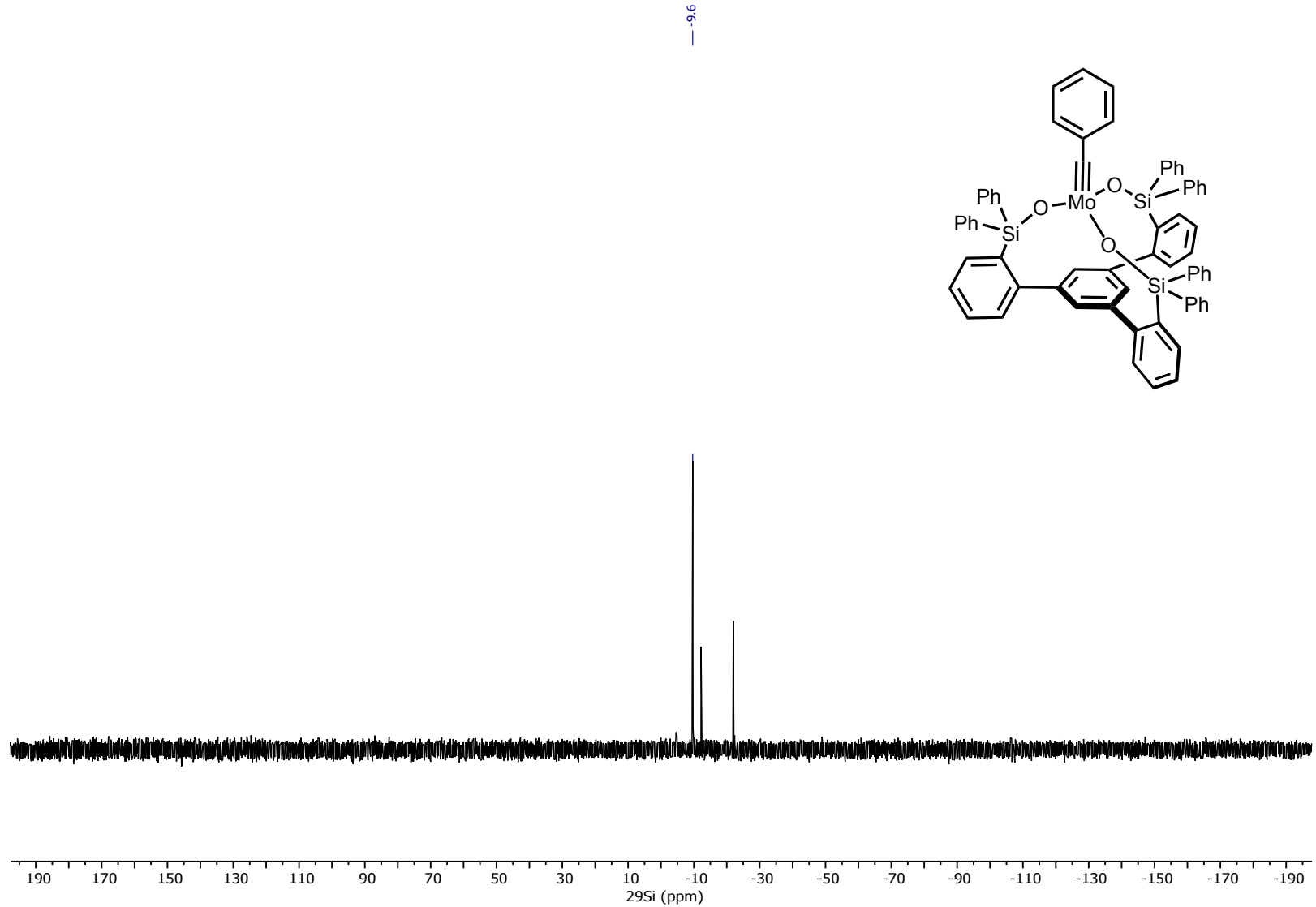
-9.6
Ph
Ph
Si
O
Mo
O
Si
Ph
Ph
O
Si
Ph
Ph
190
170
150
130
110
90
70
50
30
10
-10
-30
-50
-70
-90
-110
-130
-150
-170
-190
29Si (ppm)

^{95}Mo NMR of Complex S3, 26 MHz, $C_6D_5CD_3$, 60 °C

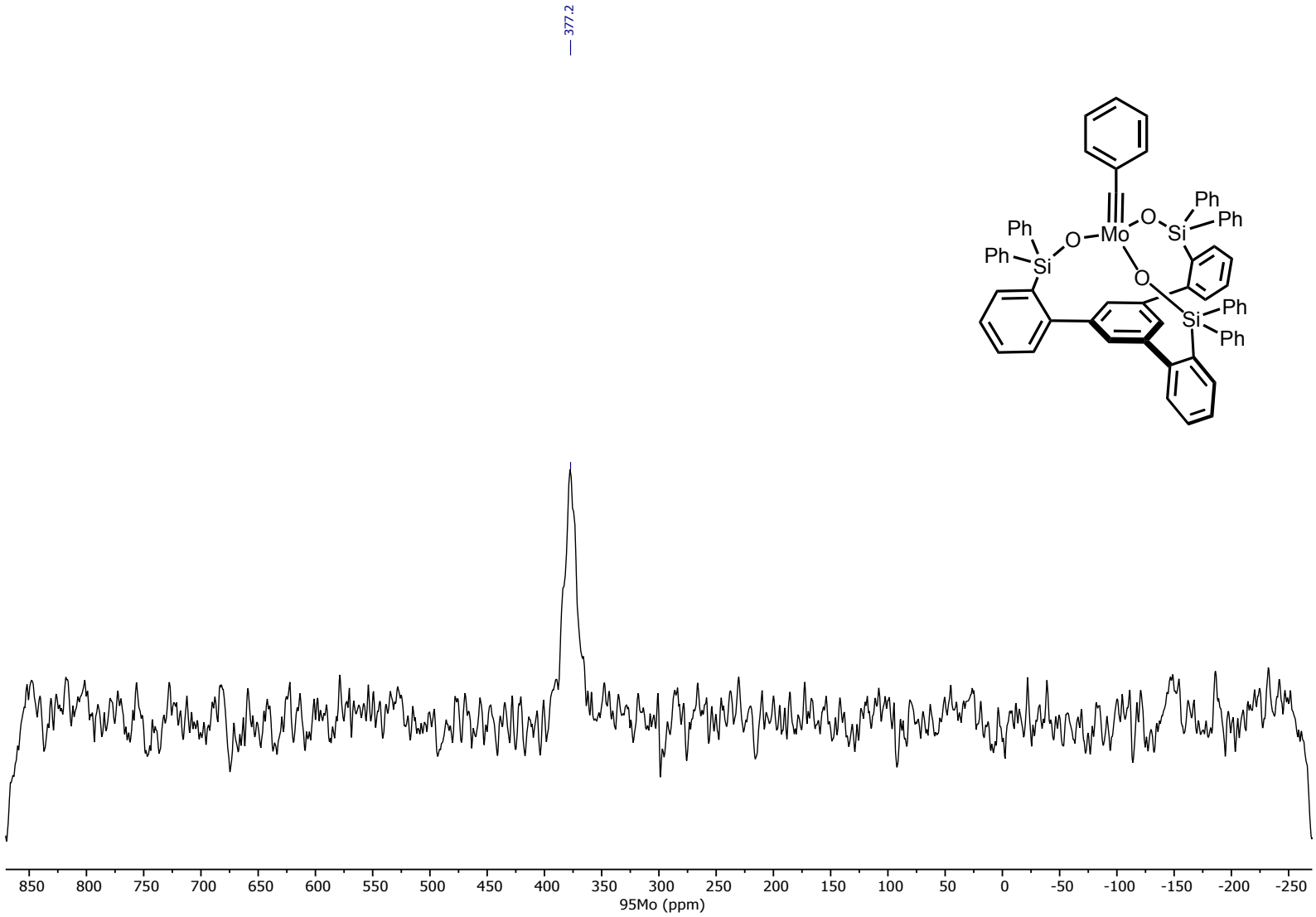

NMR characterization of 2-MTd

The sample is a complex mixture, but the following four different species could be fully characterized. Please see the next pages for the characterization data of metallatetrahedrane **2-MTd**.

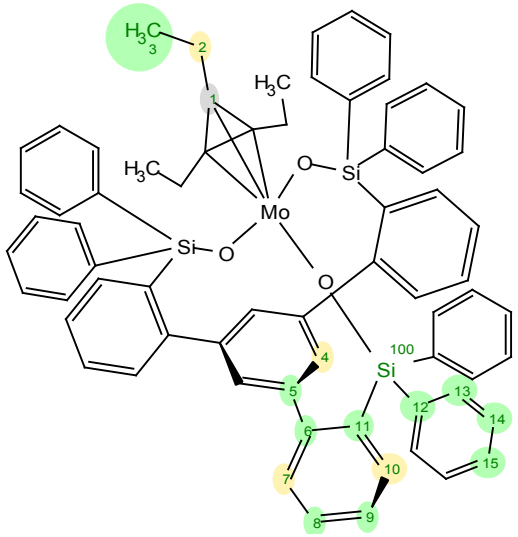

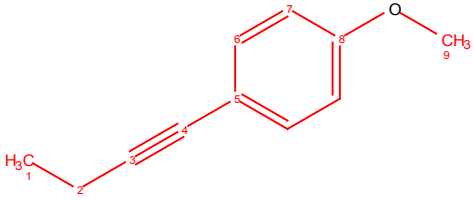

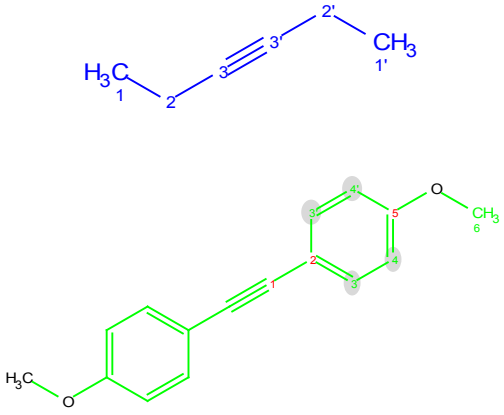

^{1}H NMR Studies of Complex 2-MTd, 600 MHz, $C_6D_5CD_3$, 25 °C

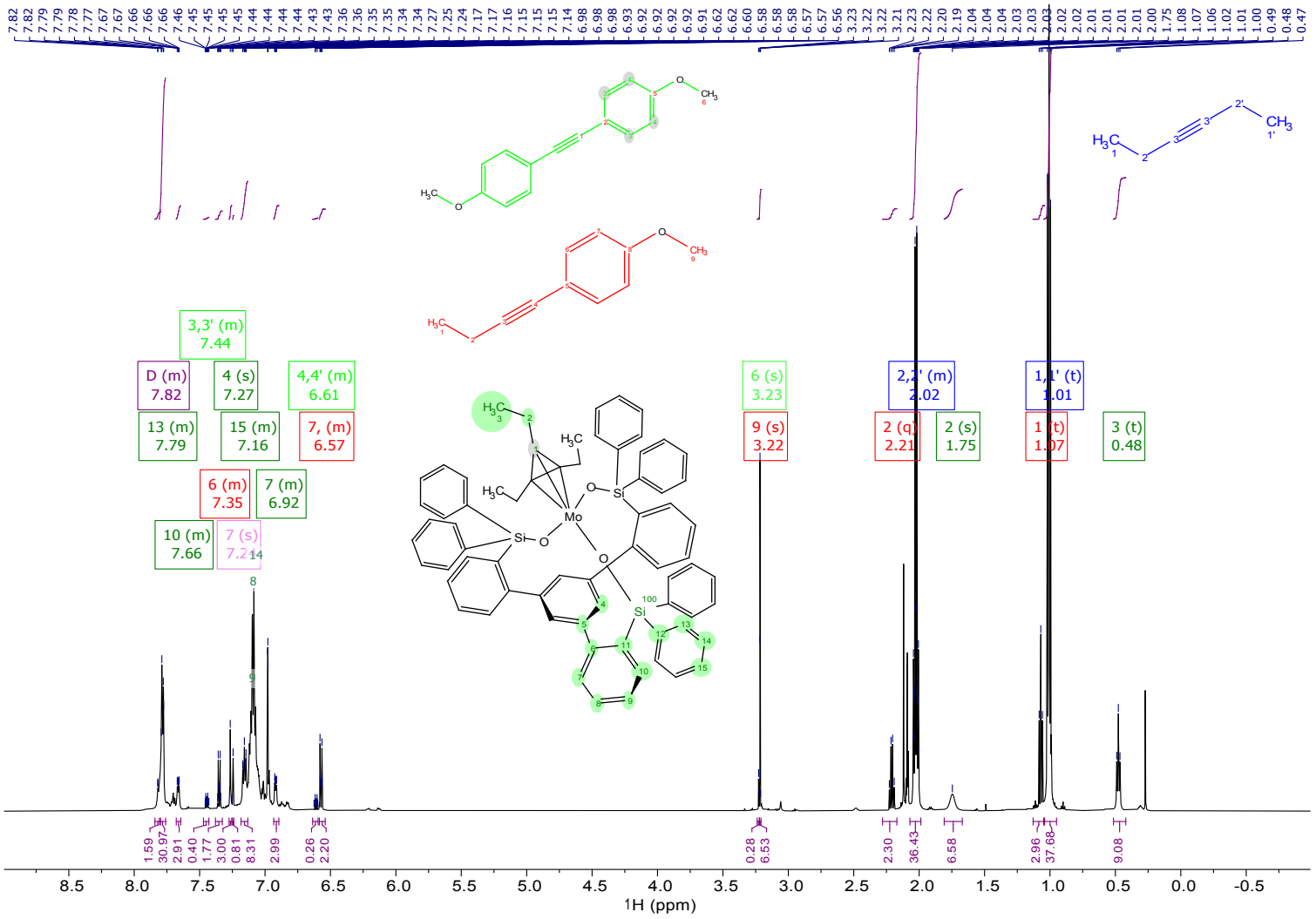

^{13}C NMR Studies of Complex 2-MTd, 151 MHz, $C_6D_5CD_3$, 25 °C

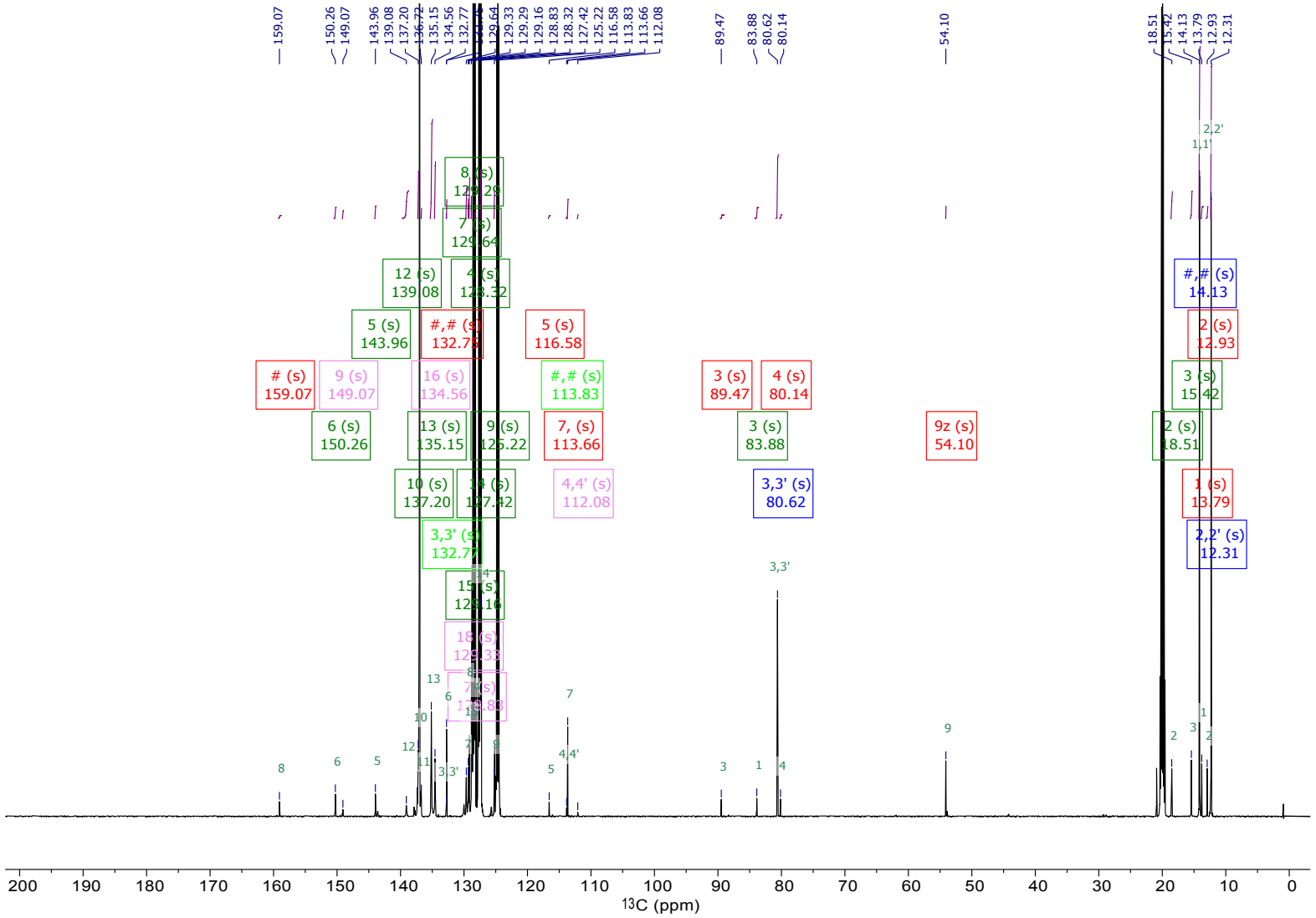

^{29}Si NMR Studies of Complex 2-MTd, 119 MHz, $C_6D_5CD_3$, 25 °C

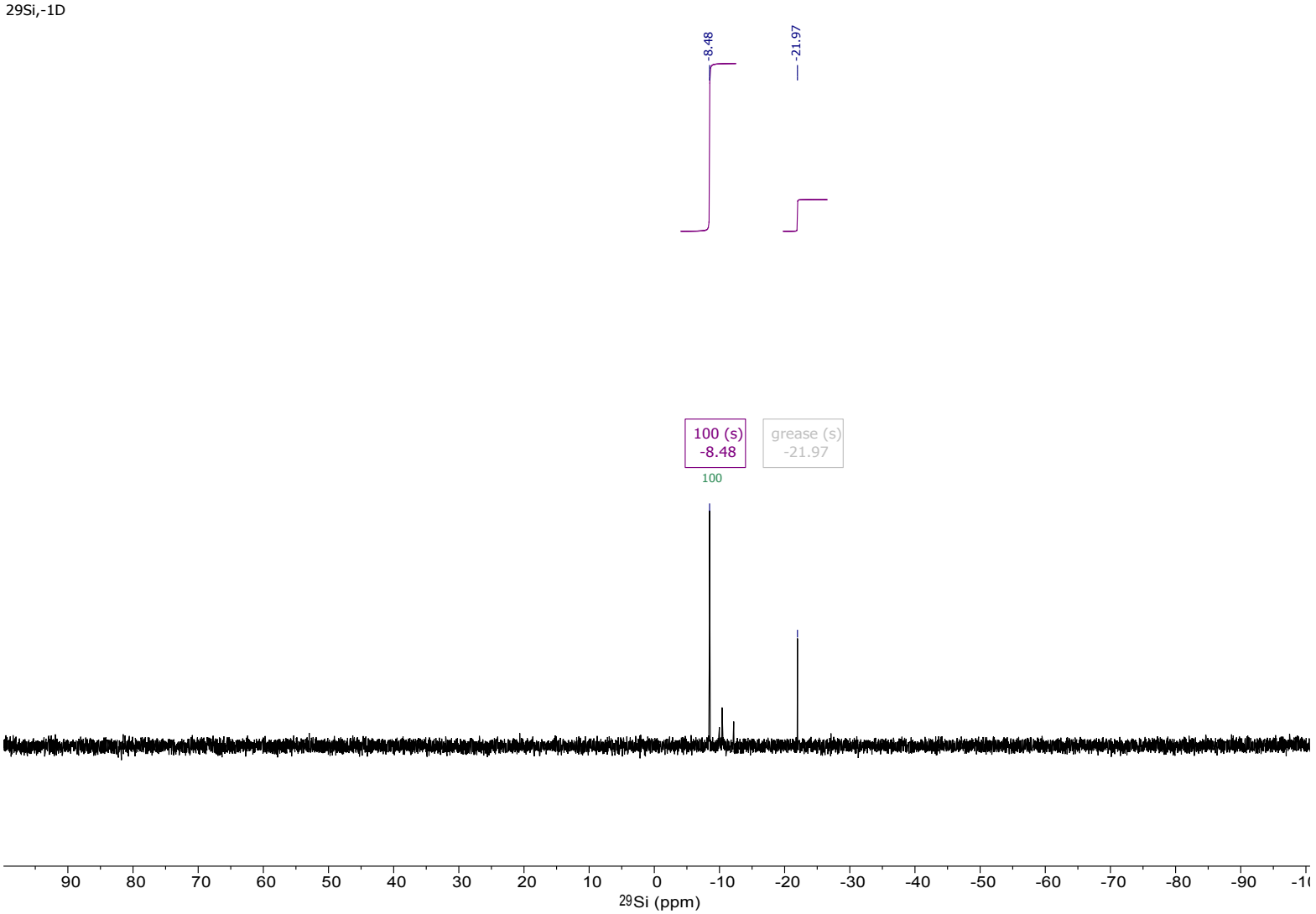

VT ^{1}H NMR Study of Complex 2-MTd, 500 MHz, $C_6D_5CD_3$, 25 °C to -70 °C

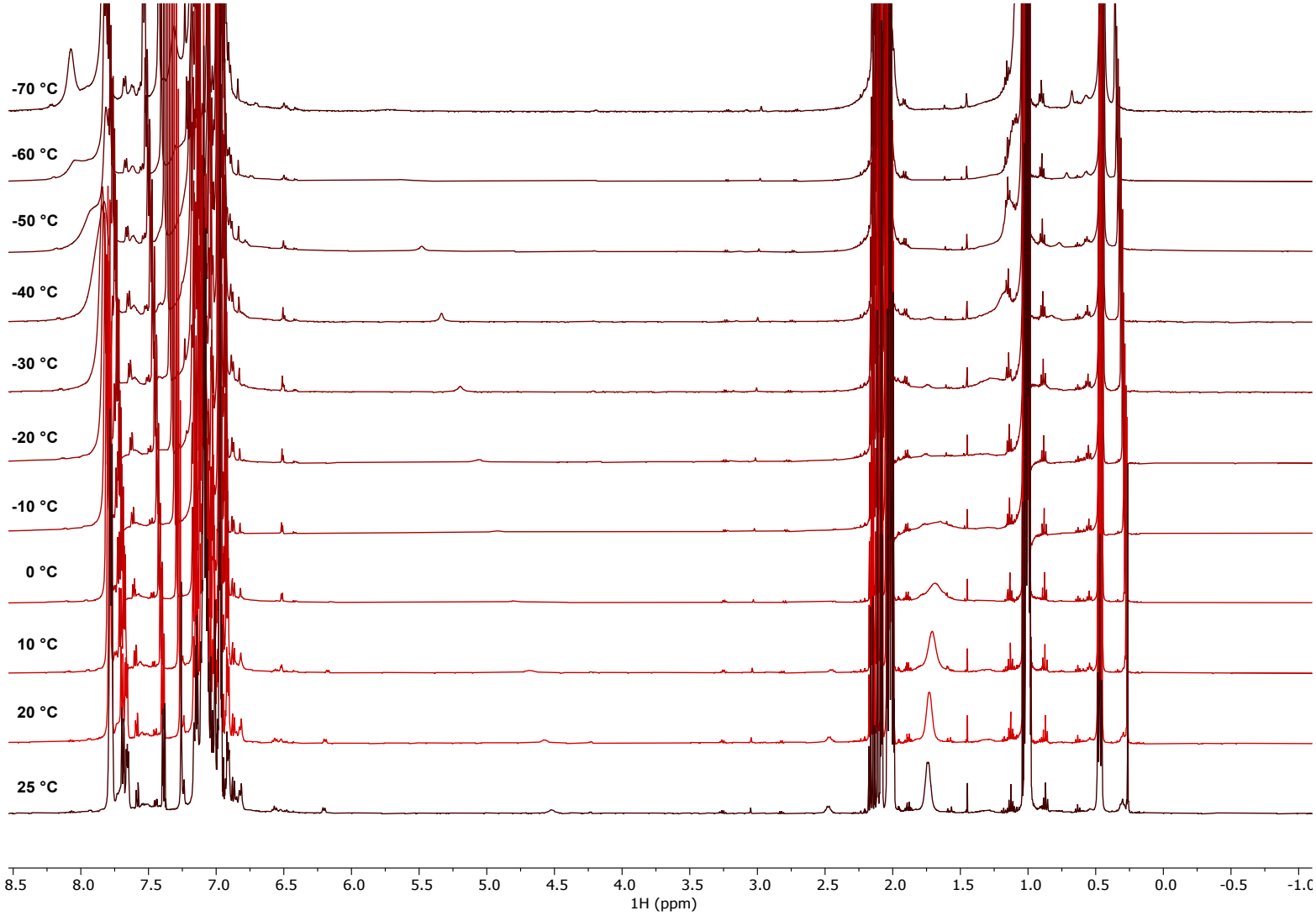

^{1}H-^{1}H NOESY NMR Study of Complex 2-MTd, 500 MHz, $C_6D_5CD_3$, 70 °C

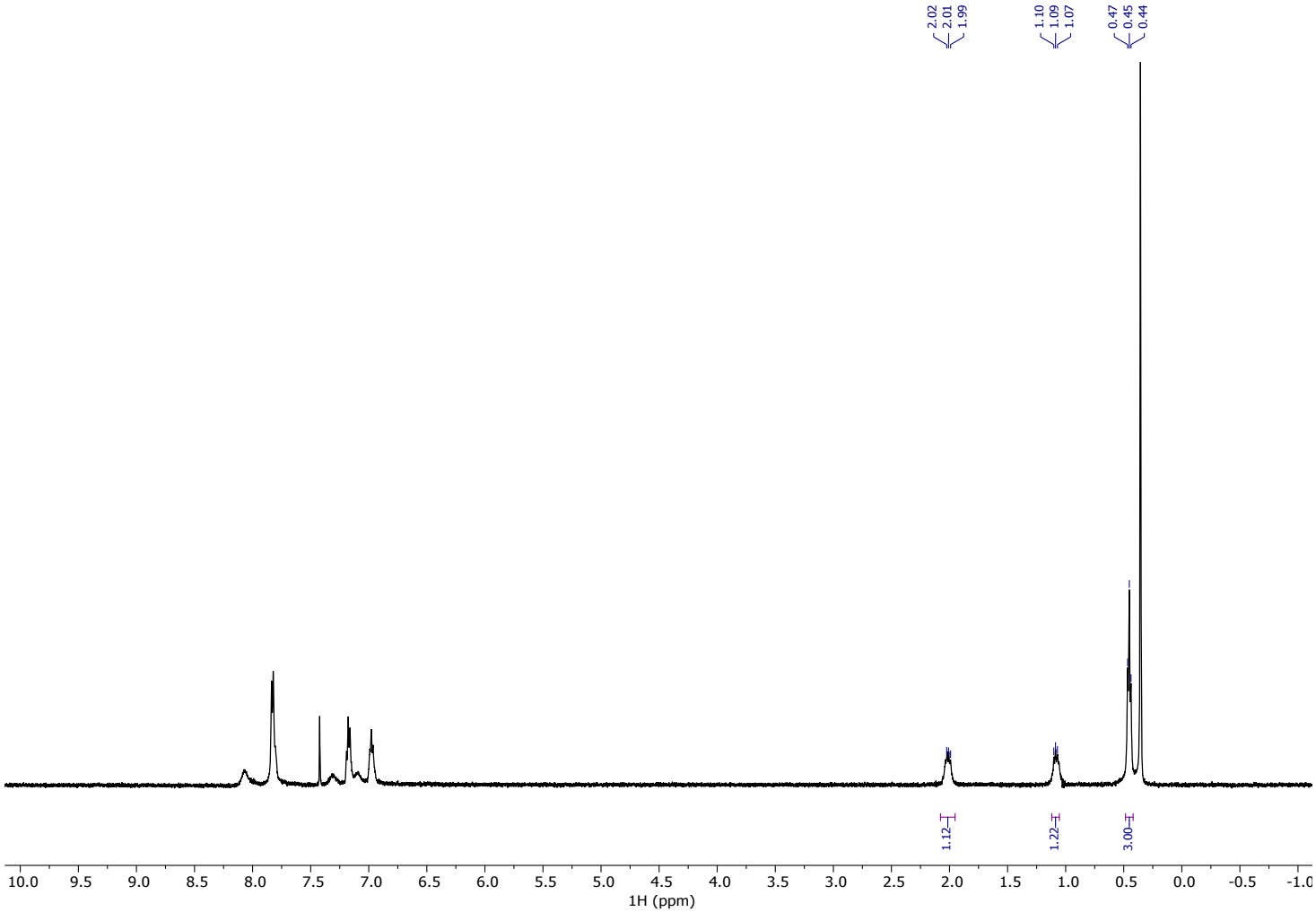
2.02
2.01
1.99
1.10
1.09
1.07
0.47
0.45
0.44
1.12
1.22
3.00
10.0 9.5 9.0 8.5 8.0 7.5 7.0 6.5 6.0 5.5 5.0 4.5 4.0 3.5 3.0 2.5 2.0 1.5 1.0 0.5 0.0 -0.5 -1.0
1H (ppm)

References

[1] Heppekausen, J.; Stade, R.; Kondoh, A.; Seidel, G.; Goddard, R.; Fürstner, A. Optimized Synthesis, Structural Investigations, Ligand Tuning and Synthetic Evaluation of Silyloxy-Based Alkyne Metathesis Catalysts. *Chem. - A Eur. J.* **2012**, *18* (33), 10281–10299. https://doi.org/10.1002/chem.201200621.

[2] Hillenbrand, J.; van Gastel, M.; Bill, E.; Neese, F.; Fürstner, A. Isolation of a Homoleptic Non-Oxo Mo(V) Alkoxide Complex: Synthesis, Structure, and Electronic Properties of Penta- Tert -Butoxymolybdenum. *J. Am. Chem. Soc.* **2020**, *142* (38), 16392–16402. https://doi.org/10.1021/jacs.0c07073.

[3] Harris, R. K.; Becker, E. D.; Cabral de Menezes, S. M.; Granger, P.; Hoffman, R. E.; Zilm, K. W. Further Conventions for NMR Shielding and Chemical Shifts (IUPAC Recommendations 2008). *Pure Appl. Chem.* **2008**, *80* (1), 59–84. https://doi.org/10.1351/pac200880010059.

[4] McCullough, L. G.; Schrock, R. R.; Dewan, J. C.; Murdzek, J. C. Multiple Metal-Carbon Bonds. 38. Preparation of Trialkoxymolybdenum(VI) Alkylidyne Complexes, Their Reactions with Acetylenes, and the x-Ray Structure of $Mo[C_3(CMe_3)_2][OCH(CF_3)_2](C_5H_5N)_2$. *J. Am. Chem. Soc.* **1985**, *107* (21), 5987–5998. https://doi.org/10.1021/ja00307a025.

[5] Thompson, R. R.; Rotella, M. E.; Du, P.; Zhou, X.; Fronczek, F. R.; Kumar, R.; Gutierrez, O.; Lee, S. Siloxide Podand Ligand as a Scaffold for Molybdenum-Catalyzed Alkyne Metathesis and Isolation of a Dynamic Metallatetrahedrane Intermediate. *Organometallics* **2019**, *38* (21), 4054–4059. https://doi.org/10.1021/acs.organomet.9b00430.